JGR Solid Earth

RESEARCH ARTICLE

10.1029/2022JB024743

Key Points:

- Experimental compaction profiles are consistent with a porosity-weakening effect predicted for grain-boundary controlled diffusion creep
- Bulk viscosities for plagioclase and olivine aggregates are three orders of magnitude lower than reported from earlier experiments
- Extrapolation to natural conditions indicates diffusion creep remains an efficient deformation mechanism in partially molten natural rocks

Correspondence to:

J. A. D. Connolly,
james.connolly@erdw.ethz.ch

Citation:

Connolly, J. A. D., & Schmidt, M. W. (2022). Viscosity of crystal-mushes and implications for compaction-driven fluid flow. *Journal of Geophysical Research: Solid Earth*, *127*, e2022JB024743. https://doi.org/10.1029/2022JB024743

Received 9 MAY 2022
Accepted 17 AUG 2022

© 2022. The Authors.
This is an open access article under the terms of the Creative Commons Attribution-NonCommercial-NoDerivs License, which permits use and distribution in any medium, provided the original work is properly cited, the use is non-commercial and no modifications or adaptations are made.

Viscosity of Crystal-Mushes and Implications for Compaction-Driven Fluid Flow

James A. D. Connolly[1] and **Max W. Schmidt**[1]

[1]Department of Earth Sciences, ETH Zurich, Zürich, Switzerland

Abstract Centrifuge experiments on olivine, chromite, and plagioclase aggregates saturated in basaltic liquid show evidence of viscous compaction by grain-boundary diffusion-controlled creep. The experiments confirm that the exponential dependence of shear viscosity on melt fraction, observed at low porosities in earlier shear deformation experiments, extends to sedimentary porosities. The compaction profiles are inconsistent with the porosity-dependence commonly ascribed to viscosity in macroscopic compaction models, which underestimate the effect of matrix disaggregation and consequently overestimate the viscosities of crystal mushes by 1–2 orders of magnitude. The time to halve the porosity of natural olivine igneous sediments by compaction is estimated from the centrifuge experiments to be $O(10^3)$y. Half-times for plagioclase and chromite layers are $O(10^4\text{–}10^5)$y, suggesting that such layers compact on magmatic time scales only if they are loaded by additional sedimentation. At conditions relevant to melt flow in asthenospheric settings and trans-crustal magmatic systems, the bulk and shear viscosities inferred for olivine and plagioclase are $O(10^{17})$ Pa s, 4 orders of magnitude less than inferred from earlier experimental studies of the diffusion creep rheology. The reduced viscosities imply time- and length-scales for compaction processes that are substantially shorter than previously anticipated. Our analysis serendipitously reveals that the oft-neglected solidity term of the Carman-Kozeny porosity-permeability relation is essential to prevent non-physical behavior in models of cumulate compaction.

Plain Language Summary The weight of the rocks overlying partially molten regions of the Earth squeezes melt toward the surface. This process is usually limited by rock viscosity and because rock viscosities are extremely high it is not easily observed. We review three sets of experiments on common crustal and mantle minerals in which melt expulsion was accelerated in a centrifuge. The results are consistent with recent theoretical models for rock viscosity and suggest that melt expulsion is substantially faster than previously anticipated.

1. Introduction

Over the past decade our laboratory has conducted centrifuge experiments in which suspensions of olivine (Schmidt et al., 2012), chromite (Manoochehri & Schmidt, 2014), and plagioclase (Krattli & Schmidt, 2021) in basaltic liquid settle and compact. We review these experiments to extract a constitutive relation for the viscosity of natural partially molten cumulates and to estimate the relevant compaction times (McKenzie, 1984). Viscosity is the most uncertain property dictating cumulate compaction and, more broadly, compaction-driven fluid flow in natural rocks. Compaction in melt-saturated olivine aggregates has been the subject of several experimental studies (Cooper et al., 1989; Daines & Kohlstedt, 1993; Renner et al., 2003), which, in combination with shear deformation experiments on partially molten olivine (Hirth & Kohlstedt, 1995; Mei et al., 2002) and plagioclase (Dimanov et al., 1998; Rybacki & Dresen, 2004) aggregates, suggest that at similar conditions to those of interest here the compaction mechanism is melt-enhanced grain-boundary diffusion-controlled creep, a category of the mechanism known more broadly as pressure-solution creep (Rutter, 1976; Shimizu, 1995; Stocker & Ashby, 1973). Extrapolation of the viscosities estimated from these experiments to natural grain sizes yields $O(10^{19})$Pa s bulk viscosities. In contrast, explanation of field observations on igneous cumulates in light of compaction theory (McKenzie, 1984) requires $O(10^{12}\text{–}10^{17})$Pa s bulk viscosities (Boudreau & Philpotts, 2002; McKenzie, 2011; Shirley, 1986; Tegner et al., 2009). The centrifuge experiments expand the range of melt fractions considered in earlier work to include those of magmatic sediments, and together with earlier results at intermediate porosities (Renner et al., 2003), reveal that the porosity-weakening trend observed in partially molten olivine aggregates (Cooper et al., 1989; Hirth & Kohlstedt, 1995; Mei et al., 2002) extends, essentially unabated,

Table 1
Frequently Used Symbols and Notation

Symbol	Meaning
α	$-\,\partial\,(\ln\eta)\,/\partial\phi$ (Equation 2)
δ, δ_0	Local viscous compaction length-scale, characteristic value (Equation 11)
ϕ, ϕ_0	Porosity, characteristic value
ϕ_{d}, ϕ_{sed}	Disaggregation porosity, sedimentary porosity
η, η_{s}, η_{f}	Matrix, solid (Equation 29), and fluid shear viscosity
ρ_{s}, ρ_{f}, $\Delta\rho$	Solid density, fluid density, $\rho_{\mathrm{s}}-\rho_{\mathrm{f}}$
τ, τ_0	Local viscous compaction time-scale, characteristic value (Equation 12)
ξ	Matrix bulk viscosity (Equation 1)
a	Centrifugal or gravitational acceleration
b	Carman-Kozeny solidity $(1-\phi)$ exponent (Equation 22)
c_k, c_η, c_ξ	Permeability coefficient (Equation 22), viscous coefficient (Equation 29), geometric factor (Equation 1)
CN	Grain coordination number
d	Grain diameter
$\mathrm{D}/\mathrm{D}t$	Material derivative $(\partial/\partial t + v_{\mathrm{s}}\,\partial/\partial z)$
f_η, f_ξ	Porosity dependence of η, residual porosity dependence of ξ
g	Magnitude of gravitational acceleration, ~ 10 m/s^2
h, h_0	Sedimentary column height, initial value
k	Matrix permeability (Equation 22)
m	Grain size exponent (Equation 29)
n, n_σ	Carman-Kozeny porosity exponent (Equation 22), rheological stress exponent
$O(10^x)$	"Of the order of 10^x"
p_{e}	Effective pressure (mean stress–fluid pressure)
q_{f}, Q	Fluid flux (Equation 21), viscous creep activation energy (Equation 29)
t, T	Time, temperature
$t_{1/2}$	Time to halve sedimentary porosity by rheologically-limited compaction
$t_{2/3}$	Time to reduce sedimentary porosity by 1/3 by hydraulically-limited compaction
v_{s}, v_{f}, v_ϕ	Solid velocity, fluid velocity, phase velocity of the porosity (Equation 24)
z	Spatial coordinate

to sedimentary porosities. This weakening effect may do much to reconcile field and experimental constraints and observations.

This paper begins with a recapitulation of the centrifuge experiments. Unlike earlier experiments (Cooper et al., 1989; Renner et al., 2003) that directly recorded compaction rates, a limitation of the centrifuge experiments is that the observed porosity profiles are the time-integrated result of the compaction process. Therefore, interpretation of the profiles requires a compaction model. To this end, we then review the relation between bulk and shear viscosity and consider its consequences for limiting compaction models. The exercise reveals that profiles obtained using conventional formulations differ substantially from those obtained using the formulation appropriate for diffusion creep (Holtzman, 2016; Rudge, 2018; Takei & Holtzman, 2009a) and that only the latter profiles are consistent with the centrifuge results. The diffusion creep formulation is then used to infer viscosities from the experiments. In the discussion, these viscosities are used to construct a deformation map that shows the viability of diffusion creep as a mechanism for natural compaction processes and to assess the time- and length-scales for compaction-driven melt flow. Notation is summarized in Table 1.

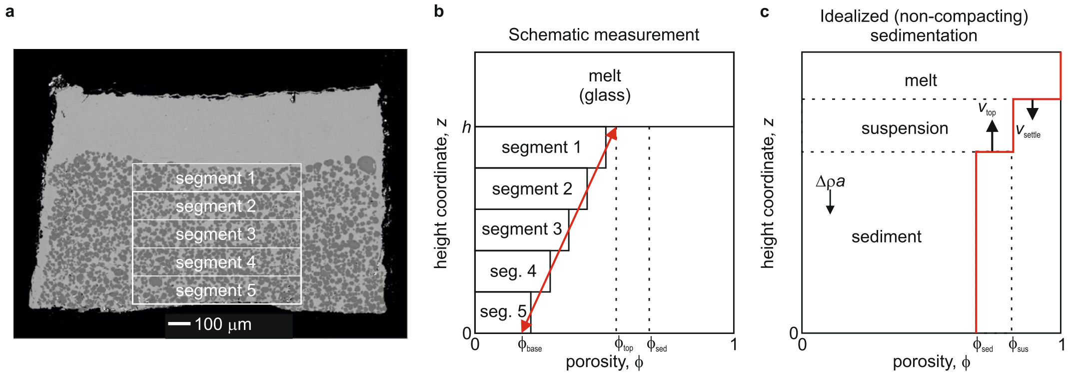

Figure 1. An axial section through olivine experiment ZOB4 (Table 2) after centrifuging (a) and schematic aspects (b) of the centrifuging experimental geometry, and interpretation (c). The spatial coordinate, *z*, system for the 1-dimensional sedimentary columns is chosen so that the product of the acceleration, *a*, and the density difference, $\Delta\rho$ ($\rho_{\text{solid}}-\rho_{\text{fluid}}$), is negative. The negative direction is referred to as downward and terms such as top, base, settling, depth, and height are used accordingly. This usage is non-standard for crystal floating experiments, but allows description of both floating and sinking experiments with a single geometric model. The origin of the spatial coordinate, $z = 0$, is placed at the base of the sedimentary column. After an experiment, the experimental charge consists of crystal free glass above a partially compacted sedimentary column. The column is divided into 4–8 virtual segments and the average porosity in each segment determined by image analysis. These porosities, and corresponding height coordinates for the center of each segment, are fit by a regression line that is extrapolated to estimate the porosity at the top, $z = h$, and base, $z = 0$, of the column. During settling of a uniform suspension of rigid crystals, the sedimentary column grows upward as a porosity shock across which the porosity increases from the sedimentary porosity, ϕ_{sed}, to the suspension porosity, ϕ_{sus}, while a second porosity shock, across which the melt fraction drops from unity to ϕ_{sus}, propagates downward from the top of the capsule. Sedimentation ceases when the two shocks meet. The resolution of the porosity in the centrifuging experiments is not adequate to resolve whether the lower shock is present in the quenched charges, however analysis suggests that with the possible exception of the GXZ54 plagioclase experiment the duration of the experiments is greater than the time predicted for complete settling by Stokes' law (Appendix A, Table 3).

2. Recapitulation and Interpretation of the Centrifuge Experiments

The minerals used as starting materials in the centrifuge experiments were Stillwater plagioclase (77 mol% anorthite), San Carlos olivine (Mg# 90.8), and a chromite (Mg# 38) from the UG3 layer of the Bushveld complex. After the experiments plagioclase had micron-thick anorthite-depleted rims with a composition of 68 mol% anorthite around a core with the original composition, and olivine (Mg# 92.2) and chromite (Mg# 48) remained homogeneous but were slightly depleted in iron. All three sets of experiments followed similar procedure. A cylindrical capsule of 0.5–1.5 mm inner radius and 1–4 mm length was loaded with a mixture of the relevant mineral, with grain sizes of 5–10 μm, and powdered basaltic glass. Raman spectroscopic examination indicated adsorbed water-content in the starting materials was below 0.2wt%. In the experiments considered here, the initial volume fraction of glass was 40% in the chromite experiments and 30% in the olivine and plagioclase experiments. The capsules were placed in a piston-cylinder apparatus and annealed at the pressure and temperature of interest for a period of 1–10 days. Annealing assured that little grain growth occurred during the subsequent, relatively short, centrifuging stage of the experiment. No detectable settling occurred during annealing, thus at the onset of centrifuging the crystal-melt mixture was homogeneous. Measured volumetric melt fractions after annealing were 74.5 ± 0.6%, 65.2 ± 0.6%, and 60.0 ± 0.4%, for plagioclase, olivine, and chromite respectively, the discrepancy between initial and annealed melt fractions in the silicate experiments is due to chemical equilibration.

For the centrifuging stage of the experiments, the samples were transferred to a smaller piston cylinder that was placed in the centrifuge so that the cylindrical axis of the sample capsule was aligned with the centrifugal acceleration. Centrifuging was of variable duration, 0.2–50 hr, and acceleration, 200–1,500 *g*. Because the piston cylinder cannot be heated unless the centrifuge is rotating, and the pressure in the piston cylinder cannot be regulated during centrifuging, the pressure recorded at the end of the centrifuging differed by as much as 20% from that of the annealing stage. After quenching, the capsules were sectioned along their cylindrical axis; hereafter, position within the sample parallel to this axis is identified as depth. In section the samples consist of a crystal-free glass layer above a partially compacted sedimentary column (Figure 1a). The sedimentary columns were divided into contiguous virtual segments and the average porosity of each segment determined by image analysis. In the

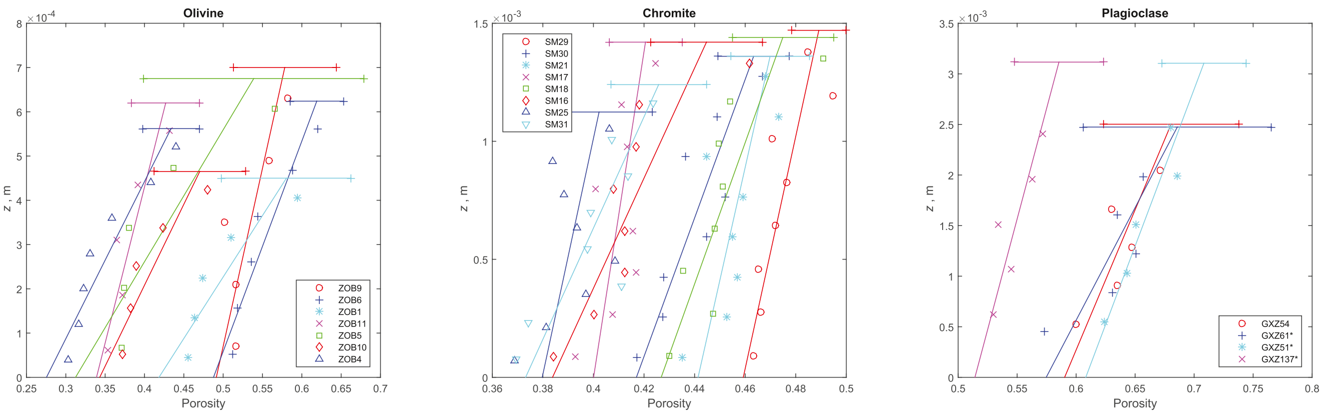

Figure 2. Experimental compaction profiles for olivine (Schmidt et al., 2012), chromite (Manoochehri & Schmidt, 2014), and plagioclase (Krattli & Schmidt, 2021); the regression lines fit to each profile are extrapolated to estimate the porosity at $z = h$ and $z = 0$. The three plagioclase experiments marked by asterisks in the legend were crystal-floating experiments. Colors have no significance other than to distinguish individual experiments. Horizontal error bars indicate a 95% confidence interval on the porosity at $z = h$, which is comparable to the confidence interval on the basal porosity.

olivine and chromite experiments, the top and bottom segments were located within a grain thickness, ~ 15 μm, of the actual top and bottom of the column. In the plagioclase experiments, the gaps between the upper- and lower-most segment and the actual top and bottom are comparable to the segment thickness, ~ 400 μm. The porosity at the true top and base of the column was estimated by linear regression of the average porosity recorded in each segment (Figures 1b and 2). Use of a non-linear regression model is not justified by the quality of the data but the linear model systematically over-predicts the measured porosities in the upper and lower tails of the profiles for the olivine experiments suggesting that the compaction process generates concave porosity profiles. That such a pattern is not evident in the chromite and plagioclase profiles may reflect that the compaction in these experiments is less extensive and therefore less well-resolved.

When a homogeneous suspension settles to form a sedimentary column the expectation is that the column grows upward as a porosity shock (Figure 1c); above the shock the porosity is the melt fraction of the suspension, ϕ_{sus}, and immediately below the shock it is the uncompacted sedimentary porosity, ϕ_{sed}. The latter is of interest because it is the porosity at which the solids grains form a coherent matrix with non-zero viscosity. In continuum compaction models ϕ_{sed} is preserved, despite the vanishing strength of the matrix, because the effective pressure responsible for compaction also vanishes at the top of the column. The variability of the estimated porosity at the top of the centrifuged samples, ϕ_{top}, inferred from linear regression (Figure 2, Table 1) is inconsistent with this expectation. Thus, ϕ_{top} cannot be taken as a proxy for the sedimentary porosity. One explanation for this discrepancy is that the uppermost portions of the experimental profiles veer to ϕ_{sed} on a spatial scale that is smaller than the thickness of the segments used for image analysis. An alternative explanation is that at the large centrifugal accelerations of the experiments, grain-scale variation in pressure may be sufficient to cause compaction in the uppermost layer of sedimented grains, effectively erasing the sedimentary porosity; subsequently, we show that this is quantitatively feasible.

In a parallel set of experiments on olivine run at similar conditions to those considered here, but with an iron-saturated Fe–S melt instead of basaltic liquid (Solferino, 2008), compaction was undetectable. Because the solubility of silicates in sulfide liquids is negligible (Kilburn & Wood, 1997), this negative observation is evidence that the viscous mechanism involves diffusive mass transport through the basaltic liquid. The number of observable grain contacts in the experiments with basaltic liquid is insufficient to prove textural equilibrium. However, substantial grain growth occurs during the annealing stage of the experiments with the result that the grains are idiomorphic and individually equilibrated with the melt at the onset of centrifuging. During compaction, the grain contacts are flattened. In the olivine samples, examination by transmission electron microscopy demonstrated unequivocally that the grain contacts are melt-free (Schmidt et al., 2012). Grain contacts in the chromite and plagioclase samples were not resolved at the atomic scale, but show no evidence of wetting by the melt at the resolution of scanning electron microscopy. In combination, the observations that presence of basaltic liquid is necessary for compaction and that grain contacts are not wetted by the melt are a compelling argument that the viscous mechanism was indeed melt-enhanced grain-boundary diffusion-controlled creep, as has been argued for earlier low-stress deformation experiments on partially molten olivine and plagioclase aggregates (Cooper et al., 1989; Dimanov et al., 1998; Hirth & Kohlstedt, 1995; Mei et al., 2002; Rybacki & Dresen, 2004). We are unaware of an experimental basis for this assumption re chromite, however the mechanism is plausible given the small grain size of the experimental charges and the stresses $O(10–100)$kPa responsible for compaction. For brevity, we refer to the mechanism subsequently as diffusion creep. Because the samples undergo a $\sim 40\%$ volume reduction during annealing the macroscopic strain associated with compaction during the experiments is not measureable. Given the relatively high strength of the solid pressure medium compared to that of a crystal suspension, and that the effective pressures responsible for compaction are four orders of magnitude below the confining pressure, we assume the compaction is macroscopically one-dimensional. The absence of textural anisotropy is attributed to effects of grain boundary sliding as a secondary deformation mechanism (Faul & Jackson, 2007).

3. Relation Between Bulk and Shear Viscosity

As the bulk viscosity of individual solid grains is infinite on geologically relevant time scales (Glatzmaier, 1988), the bulk viscosity of a porous matrix composed of solid grains, ξ, must ultimately be related to its shear viscosity and porosity. We generalize this relation as

$$\xi = c_\xi f_\xi f_\eta \eta_\mathrm{s} \tag{1}$$

where c_ξ is a geometric constant, f_η and f_ξ are functions of porosity, η_s is the shear viscosity of the matrix in the limit $\phi \to 0$ such that the shear viscosity at finite porosity is $\eta = \eta_\mathrm{s} f_\eta$, and f_ξ is any residual porosity dependence of the bulk viscosity, referred to hereafter simply as the porosity dependence of the bulk viscosity. In the case of non-linear viscous mechanisms, such as dislocation creep, ξ, η, and η_s, are properly identified as effective viscosities; for brevity, license is taken to refer to these parameters simply as viscosities when the distinction is of no consequence. Our formulation identifies ξ and η as properties of the solid matrix rather than as properties of the solid-melt aggregate. In the limit that the melt shear viscosity is negligible in comparison to that of the solid, this distinction is unimportant. When this limit is not relevant more elaborate mixture theories are required to describe the viscosities of the solid-melt aggregate (Keller & Suckale, 2019). In both diffusion and dislocation creep regimes at $O(0.01)$ melt fractions, shear viscosity varies strongly and inversely with porosity (Cooper & Kohlstedt, 1984), a dependence often characterized empirically as

$$f_\eta = \exp(-\alpha\phi) \tag{2}$$

where α, the negative of the logarithmic derivative of the shear viscosity with respect to porosity, is approximated as an empirical constant in the range 25–30 for diffusion creep (Hirth & Kohlstedt, 2003). The constant α model is unsatisfactory both in that α is observed to decrease at $O(0.1)$ melt fractions (Hirth & Kohlstedt, 1995, 2003; Mei et al., 2002) and that α must become infinite as melt fractions approach the disaggregation limit, ϕ_d, at which grains of the matrix are completely wetted by the melt and the shear viscosity of the matrix vanishes. This variation in α is reproduced qualitatively by theoretical models of diffusion creep that distill to the first order approximation (Rudge, 2018; Takei & Holtzman, 2009a)

$$f_\eta^\mathrm{dif} = \left(1 - \sqrt{\phi/\phi_\mathrm{d}}\right)^2. \tag{3}$$

The basis of this approximation is that increasing porosity increases the rate of viscous deformation by diffusion creep because it both increases grain-contact stress and shortens the path length for grain boundary diffusion (Cooper et al., 1989). Both effects are expected to vary as the fraction of the grain-to-grain contact relative to the total grain surface area, which is approximated as $1 - \sqrt{\phi/\phi_\mathrm{d}}$. In detail, f_η^dif does not reproduce the large values of α measured at $O(10^{-2})$ porosities, but it emerges that it is adequate at higher porosity. The deficiency at small porosity is of little consequence here because extrapolation of f_η^dif over the low porosity interval, where larger α values may be relevant, affects η_s by less than a factor of 2, an effect that is comparable to the accuracy of rheological measurements. An implicit assumption in Equation 3 is that grain coordination number (CN) does not vary with porosity. This assumption is reasonable for scenarios in which a rock ($CN \approx 12$) undergoes decompaction by partial melting or melt infiltration but is implausible for compaction of igneous sediments, where the high porosities observed here imply an initial $CN \approx 6$ (Hilbert & Cohn-Vossen, 1952). While it is possible to account for the variation in *CN* during compaction (Swinkels et al., 1983) the resulting formulations are cumbersome and lack generality. Here we note only that such an accounting would lead to more rapid strengthening than anticipated by Equation 3.

Both ϕ_d and ϕ_sed represent the porosity of the transition between fluidized suspension and coherent matrix. They are distinguished because ϕ_d defines the transition in aggregates with initially high grain *CN* and is therefore largely determined by wetting properties, whereas ϕ_sed represents the transition during sedimentation and is likely primarily dependent on grain shape and the settling process. Thus, ϕ_d and ϕ_sed must be interchanged depending on the process under consideration. Extrapolation of the linear relation between the number of grain boundaries wetted with porosity observed at low porosity (< 0.1, Hirth & Kohlstedt, 1995; Mei et al., 2002) places a lower bound on ϕ_d of 0.22–0.33 for texturally equilibrated olivine-MORB aggregates. Models for the entire range of porosity (Rudge, 2018; Takei & Holtzman, 2009a) indicate larger values, ≈ 0.4, are relevant.

Models of grain-boundary limited diffusion creep give $\xi^\mathrm{dif} = c_\xi^\mathrm{dif}\eta^\mathrm{dif}$, that is, $f_\xi^\mathrm{dif} = f_\sigma^\mathrm{dif} = 1$. The factor c_ξ^dif is weakly dependent on grain shape (Cooper et al., 1989; Rudge, 2018; Takei & Holtzman, 2009a) but is taken as a constant of $\frac{5}{3}$ hereafter. The simple behavior of diffusion creep contrasts with that of dislocation creep for which bulk viscosity is a strong function of porosity (Wilkinson & Ashby, 1975)

$$f_\xi^\mathrm{dis} = \frac{\left(1 - \phi^{1/n_\sigma}\right)^{n_\sigma}}{\phi(1-\phi)} \tag{4}$$

that becomes infinite in limit $\phi \to 0$, where n_σ is the power-law stress exponent for the mechanism and, for tubular pores,

$$c_\xi^\mathrm{dis} = \frac{3}{2}(n_\sigma/2)^{n_\sigma}. \tag{5}$$

In its linear-viscous limit, $n_\sigma \to 1$, Equation 5 evaluates to $c_\xi^\mathrm{dis} = \frac{3}{4}$; for alternative pore geometries c_ξ^dis remains $O(1)$ (Schmeling et al., 2012). The arguments that justify the porosity dependence of the diffusion creep shear viscosity imply that for dislocation creep (Mei et al., 2002)

$$f_\eta^\mathrm{dis} = \left(1 - \sqrt{\phi/\phi_\mathrm{d}}\right)^{n_\sigma} = \left(f_\eta^\mathrm{dif}\right)^{n_\sigma/2}. \tag{6}$$

In the large porosity limit, $\phi \to \phi_\mathrm{d}$, Equation 6 is well-approximated by $f_\eta^\mathrm{dis} \approx (1 - \phi/\phi_\mathrm{d})^{n_\sigma}$.

In distinction to the above relations, in macroscopic compaction formulations (e.g., Bercovici et al., 2001; McKenzie, 1984; Scott & Stevenson, 1984) the matrix shear viscosity is usually (cf., Connolly & Podladchikov, 2015; Dohmen et al., 2019) ascribed the porosity dependence

$$f_\eta^\mathrm{lin} = 1 - \phi \tag{7}$$

and the porosity dependence of the bulk viscosity is either neglected or taken to be of the form $f_\xi = c_\xi/\phi$ which follows if the solid grains of the matrix deform as a Newtonian fluid (Nye, 1953). Although grain-size sensitive mechanisms such as diffusion creep may result in a macroscopically Newtonian matrix rheology, on the grain-scale such mechanisms are not Newtonian (Rudge, 2018, 2021; Takei & Holtzman, 2009a). Peculiarly, in its linear limit, dislocation creep ($n_\sigma \to 1$ in Equations 4 and 5) is Newtonian and results in the $f_\xi = c_\xi/\phi$ form, hence we identify this form as that appropriate to linear dislocation creep. We are aware of no geological materials that deform by linear dislocation creep but a case can be made that in rocks undergoing simultaneous compaction and macroscopic shear by dislocation creep the compaction rheology is essentially linear viscous (Tumarkina et al., 2011).

Although the influence of the porosity dependence of the bulk viscosity is minor at the large porosities of the centrifuge experiments, we show subsequently that the experimental results are inconsistent with the linear porosity-weakening shear viscosity (Equation 7) commonly adopted for macroscopic compaction models. To this end we consider three models for the bulk viscosity: “Diffusion” ($f_\xi = 1$; $c_\xi = c_\xi^\mathrm{dif} = \frac{5}{3}$; $f_\eta = f_\eta^\mathrm{dif}$, Equation 3); “Linear-Weakening” ($f_\xi^\mathrm{lin} = 1$; $c_\xi = c_\xi^\mathrm{dif}$; $f_\eta = f_\eta^\mathrm{lin}$, Equation 7); and “Dislocation” ($n_\sigma = 1$, $f_\xi = f_\xi^\mathrm{dis}$, Equation 4; $c_\xi = c_\xi^\mathrm{dis} = \frac{3}{4}$, Equation 5; $f_\eta = f_\eta^\mathrm{lin}$, Equation 7). It is apparent that the Linear-Weakening and Dislocation models are flawed in that they cannot reproduce the assumption that the matrix viscosities vanish at $\phi = \phi_d$ when $\phi_d < 1$. Despite this consideration, the simplification, or the stronger form $f_\eta = 1$, has been introduced in all macroscopic models of viscous sedimentary compaction and crystal mushes of which we are aware (Birchwood & Turcotte, 1994; Boudreau & Philpotts, 2002; Connolly & Podladchikov, 2000; Fowler & Yang, 1999; Jackson et al., 2018; McKenzie, 1985, 1987, 2011; Shirley, 1986; Solano et al., 2014; Sparks et al., 1985; Suetnova & Vasseur, 2000; Sumita et al., 1996). Our intention in considering the flawed Linear-Weakening and Dislocation models is twofold: to demonstrate that the resolution of the centrifuge compaction profiles is sufficient to invalidate them; and to demonstrate that the assumption has significant consequences for the time-scales and viscosities inferred from natural or experimental observations.

The porosity dependence of the bulk viscosity has its greatest effect at the small porosities relevant to melt transport. In this regard, microscopic models for compaction by Nabarro-Herring creep, a plausible geological mechanism at high temperature, give rise to an inverse logarithmic porosity-dependence (Arzt et al., 1983; McKenzie, 2011; Rudge, 2018). Such a porosity dependence is not considered here because it is intermediate between those of the Dislocation and Diffusion models.

4. Rheologically and Hydraulically-Limited Compaction Profiles

Compaction admits two limiting regimes: a rheologically-limited regime in which the compaction rate is dictated by the strength of the solid matrix and a hydraulically-limited regime in which the compaction rate is dictated by drainage of the interstitial fluid (Connolly & Podladchikov, 2000; McKenzie, 1984; Shirley, 1986; Sumita et al., 1996). Because the shear viscosity of the matrix modeled by Equation 3 vanishes at the sedimentary porosity, the onset of compaction must be hydraulically-limited. Dimensional argument (Appendix A) suggests that for plausible viscosities this initial hydraulically-limited phase will occur on a time-scale that is short compared to the duration of the experiments so that the initial regime evolves rapidly toward the rheologically-limited regime. On this basis, we ignore the complexity associated with such a transition and consider only the limiting cases as models for the compaction profiles (cf., Keller & Suckale, 2019).

For viscous compaction, the bulk strain rate of a porous matrix is

$$\frac{1}{1-\phi}\frac{\mathrm{D}(1-\phi)}{\mathrm{D}t} = \frac{p_\mathrm{e}}{\xi} \tag{8}$$

where: ϕ, t, and p_e are, respectively, porosity, time, and effective pressure; and $\mathrm{D}/\mathrm{D}t$ is the material derivative (Table 1). In rheologically-limited compaction, it is supposed that a sedimentary column of height h is hydrostatically loaded, in which case for 1-dimensional compaction (Fowler & Yang, 1999; Scott & Stevenson, 1986; Takei & Katz, 2013) the effective pressure is

$$p_e = \frac{\Delta\rho a}{\left(1 + \frac{4}{3}\eta/\xi\right)} \int_{z'=h}^{z'=z} (1-\phi)\,dz' \tag{9}$$

where $\Delta\rho$ is the solid density minus the fluid density, a is the gravitational or centrifugal acceleration, and the orientation of the spatial coordinate z-axis is chosen so that $\Delta\rho a < 0$. This direction is referred to as downward and, hereafter, terms such as top, base, settling, depth, and height are used accordingly (Figure 1c). This language is peculiar for crystal floating experiments, but allows description of both floating and sinking experiments with a single geometric model. The origin of the spatial coordinate, $z = 0$, is placed at the base of the sedimentary column. Substituting Equations 1 and 9, into Equation 8 and rearranging, the governing equation for the rheologically-limited regime is

$$\frac{\mathrm{D}\phi}{\mathrm{D}t} = \frac{-(1-\phi)\Delta\rho a}{\eta_\mathrm{s} f_\eta \left(c_\xi f_\xi + \frac{4}{3}\right)} \int_{z'=h}^{z'=z} (1-\phi)\,dz'. \tag{10}$$

Equation 10 is made non-dimensional by scaling the spatial coordinate by the viscous compaction length

$$\delta_0 = \sqrt{\frac{k_0 \eta_\mathrm{s} f_{\eta 0}\left(c_\xi f_{\xi 0} + \frac{4}{3}\right)}{\eta_\mathrm{f}}} \tag{11}$$

and time by the viscous compaction time

$$\tau_0 = \frac{\eta_\mathrm{s} \phi_0 f_{\eta 0}\left(c_\xi f_{\xi 0} + \frac{4}{3}\right)}{(1-\phi_0)\,\delta_0 |\Delta \rho a|} \tag{12}$$

where k is the matrix permeability, η_f is the fluid viscosity, and the subscript 0 denotes properties or functions at the characteristic porosity ϕ_0 (McKenzie, 1984). Because $f_\eta^\mathrm{dif} = 0$ at ϕ_sed, we take $\phi_0 = \phi_\mathrm{sed}/2$ and compute compaction profiles for the Diffusion, Linear-Weakening, and Dislocation models formulated in Section 3 by numerically integrating the non-dimensional form of Equation 10 by the finite difference method with lagged spatial coordinates such that after each time-step the spatial coordinates of the material elements are adjusted to satisfy continuity and the condition that base of the column is immobile. The singularity at ϕ_sed, is avoided by setting the initial porosity to 0.999 ϕ_sed. For an instantaneously sedimented column, the rheologically-limited compaction regime is expected to develop if $h_0 << \delta_0$ (McKenzie, 1984), accordingly the profiles for these models are for $h_0 = \delta_0/10$ (Figure 3).

The Linear-Weakening and Dislocation models initially develop convex profiles, though with time the Dislocation profile changes curvature at depth; both contrast with the strongly concave profiles of the Diffusion model. The time-dependence of the models is also distinctive in that the height of the sedimentary column varies as $\sim t^{-1/3}$ for the Diffusion model, $\sim t^{-1/2}$ for the Dislocation model, and $\sim t^{-1}$ for the Linear-Weakening model; the time intervals between successive profiles in Figure 3 have been chosen to illustrate these dependences. In the Diffusion model, the local value of the compaction length initially grows super-exponentially with both time and depth so that by $t = 10^{-3}\tau_0$ (Figure 3b) the local compaction length throughout the column is comparable to the column height. This behavior supports the assumption that the initial phase of hydraulically-limited compaction is of short duration and leaves the column with reduced, but nearly uniform, porosity.

The non-linearity of the compaction equations has the consequence that there is no obvious expression relating the compaction time-scale to the time required to reduce the average porosity of an instantaneously sedimented layer to a particular value. To further clarify the consequences of the porosity dependence we have numerically computed the time, $t_{1/2}$, required to halve the average porosity of a sediment layer by rheologically-limited compaction (Figure 4). By considering the linear logarithmic dependence of $t_{1/2}/\tau_0$ on h_0/δ_0 (McKenzie, 1985) and the nearly quadratic dependence of $\ln(t_{1/2}/\tau_0)$ on ϕ_sed these results collapse to

$$t_{1/2}^\mathrm{dif} \approx \frac{\delta_0^\mathrm{dif} \tau_0^\mathrm{dif}}{h_0} 0.91 e^{2.57\phi_\mathrm{sed}^2} \tag{13}$$

$$t_{1/2}^\mathrm{lin} \approx \frac{\delta_0^\mathrm{lin} \tau_0^\mathrm{lin}}{h_0} 2.42 e^{2.62\phi_\mathrm{sed}^2} \tag{14}$$

$$t_{1/2}^\mathrm{dis} \approx \frac{\delta_0^\mathrm{dis} \tau_0^\mathrm{dis}}{h_0} 2.07 e^{2.69\phi_\mathrm{sed}^2} \tag{15}$$

which reproduce the numerical values of $\log_{10}(t_{1/2}/\tau_0)$ to better than 1% accuracy. Equations 13–15 are potentially deceptive in that the compaction scales differ for each model, to facilitate comparison we note

$$\frac{\delta_0^\mathrm{lin}\tau_0^\mathrm{lin}}{\delta_0^\mathrm{dif}\tau_0^\mathrm{dif}} = \frac{f_\eta^\mathrm{lin}\left(c_\xi^\mathrm{lin} f_\xi^\mathrm{lin} + \frac{4}{3}\right)}{f_\eta^\mathrm{dif}\left(c_\xi^\mathrm{dif} f_\xi^\mathrm{dif} + \frac{4}{3}\right)} = \frac{(1-\phi_0)}{\left(1-\sqrt{\phi_0/\phi_\mathrm{sed}}\right)^2} \tag{16}$$

$$\frac{\delta_0^\mathrm{dis}\tau_0^\mathrm{dis}}{\delta_0^\mathrm{dif}\tau_0^\mathrm{dif}} = \frac{(16\phi_0 + 9)(1/\phi_0 - 1)}{36\left(1-\sqrt{\phi_0/\phi_\mathrm{sed}}\right)^2} \tag{17}$$

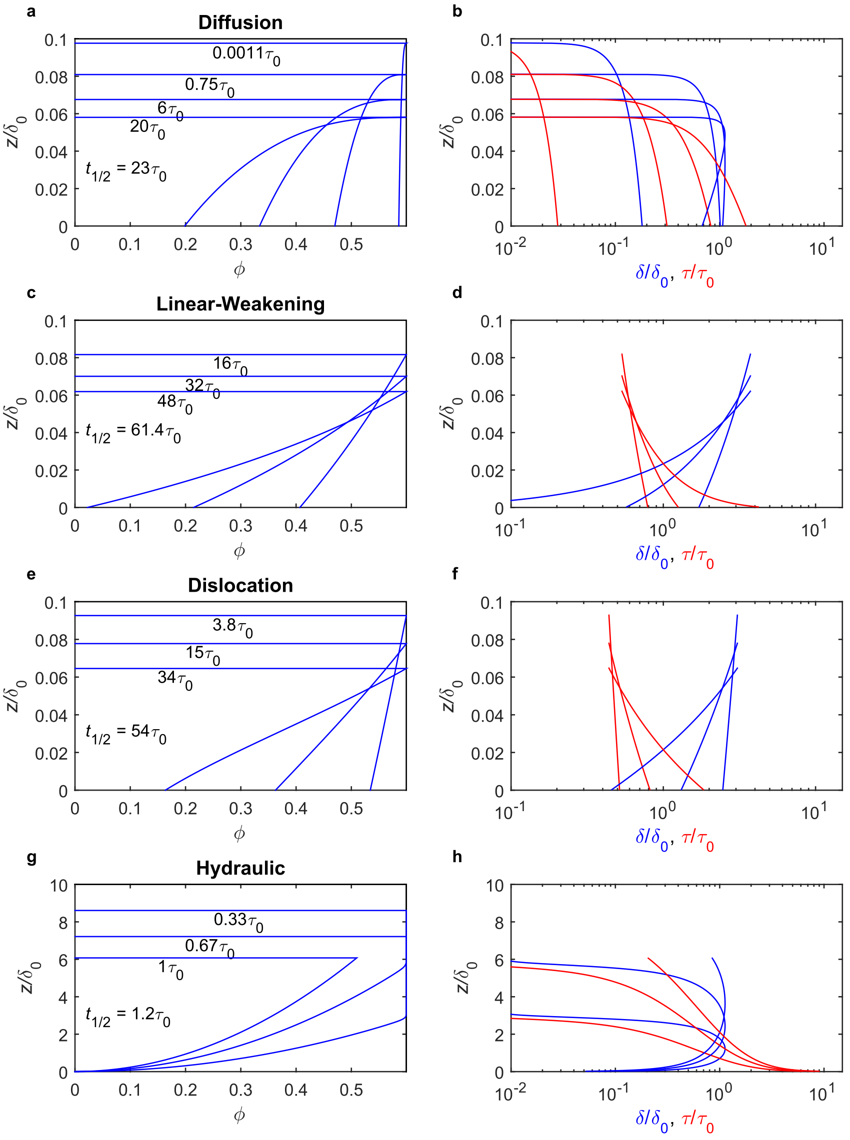

Figure 3. Computed rheologically and hydraulically-limited compaction profiles, and the corresponding local compaction time- and length-scales, for a sedimentary column with initial porosity $\phi_{\text{sed}} = 0.6 = 2\phi_0$. Three models for the porosity dependence of the bulk viscosity, as outlined in the text, are illustrated: Diffusion (a and b), Linear-Weakening (c and d), and Dislocation (e and f). All three cases are for $h_0 = \delta_0/10$; because δ_0 and τ_0 are model-dependent, the three cases do not represent columns with identical initial height. Specifically, all other factors being equal, the absolute initial height of the Diffusion model is 2.9 times greater than that of the Linear-Weakening model and 3.3 times greater than that of the Dislocation model. The same relations apply to the time-scales. Thus, the indicated times to halve the average porosity, $t_{1/2}$, are for sedimentary columns with substantially different absolute dimensions. If the models are calculated for sedimentary columns with the same absolute dimensions and physical parameters, the compaction half-times for the Diffusion model are about 20–30 times shorter than for the Linear-Weakening (Equation 18) and 20–50 times shorter than for the Dislocation (Equation 19) model. The hydraulically-limited case (g and h) is scaled by δ_0 and τ_0 for the Diffusion model with $h_0 = 10\delta_0$.

and, substituting $\phi_0 = \phi_{\text{sed}}/2$ and Equations 16 and 17, respectively, into Equations 14 and 15, obtain

$$\frac{t_{1/2}^{\text{lin}}}{t_{1/2}^{\text{dif}}} \approx 15.5\,(2-\phi_{\text{sed}})\,e^{0.05\phi_{\text{sed}}^2} \tag{18}$$

$$\frac{t_{1/2}^{\text{dis}}}{t_{1/2}^{\text{dif}}} \approx 0.73\,(9+8\phi_{\text{sed}})\,(2/\phi_{\text{sed}}-1)\,e^{0.12\phi_{\text{sed}}^2}. \tag{19}$$

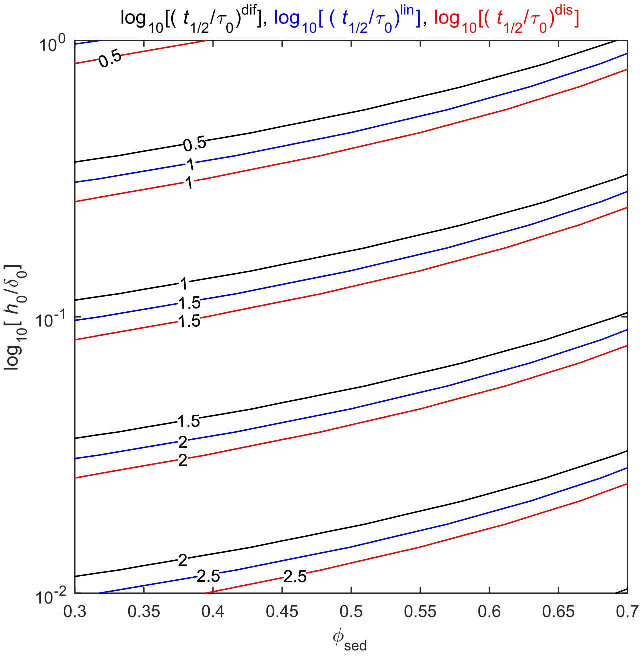

Figure 4. The log of the time to halve the average porosity of an instantaneously accumulated sedimentary layer by rheologically-limited compaction as a function of ϕ_{sed} and h_0 (logarithmic scale) for the Diffusion (black), Linear-Weakening (blue), and Dislocation (red) models. The column height and compaction times are relative to the compaction time and length scale specific to each model. When the results are fit to a common scale (Equations 18 and 19), it emerges that the compaction half-times for the Diffusion model are 20–50 times shorter than for the Linear-Weakening and Dislocation models for columns with the same absolute dimensions and physical properties.

Thus, for h_0 and ϕ_{sed} in the respective ranges 0.01–1 δ_0 and 0.3–0.7, the Diffusion model compacts about 20–30 times faster than the Linear-Weakening model and 20–50 times faster than the Dislocation model.

The governing equation for the one-dimensional hydraulically-limited regime (Connolly & Podladchikov, 2000) follows from mass conservation, which requires

$$\frac{1}{1-\phi}\frac{\mathrm{D}(1-\phi)}{\mathrm{D}t} = -\frac{\partial q_{\mathrm{f}}}{\partial z} \tag{20}$$

where q_{f} is the fluid flux given by Darcy's law in the limit $p_{\mathrm{e}} \to 0$ as

$$q_{\mathrm{f}} = \phi\left(v_{\mathrm{f}} - v_{\mathrm{s}}\right) = -\frac{k}{\eta_{\mathrm{f}}}(1-\phi)\Delta\rho a. \tag{21}$$

We assume the porosity dependence of the matrix permeability is given by the Carman-Kozeny relation

$$k = \frac{d^2}{c_k}\frac{\phi^n}{(1-\phi)^b} \tag{22}$$

where d is grain size and c_k is a factor accounting for grain geometry. Formally, the exponents n and b in the Carman-Kozeny relation have the values three and two, respectively, but in compaction literature the latter is often set to zero. Making use of Equations 21 and 22, Equation 20 can be rearranged as

$$\frac{\partial\phi}{\partial t} + v_\phi\frac{\partial\phi}{\partial z} = 0 \tag{23}$$

where

$$v_\phi = \frac{q_{\mathrm{f}}}{\phi}(n(1-\phi) + (b-1)\phi) \tag{24}$$

is the phase velocity of the porosity. For the initial conditions chosen here, in which a sedimentary column is instantaneously deposited on an impermeable substrate, solutions to Equation 23 in which v_ϕ and q do not have the same sign are non-physical. Thus, from Equation 24, if $n > 0$, then $b \geq 1$ is a physical constraint on Equation 22 in the limit $\phi \to \phi_{\mathrm{sed}}$. In this limit, the difference between the velocities of the solid grains and fluid predicted by Darcy's law must be identical to the settling velocity of a suspension with solid fraction ϕ_{sed}. As this limit is relevant here, we force consistency between Equations 21 and 22 and Stokes' law (Equation A2 with $s = 0$) by taking $b = 1$ and $c_k = 18$, and take $n = 3$, as in the original formulation of the Carman-Kozeny relation. The value for c_k lies within the range 3–27 measured for Darcyian flow at $\phi << \phi_{\mathrm{sed}}$ in a set of centrifuge experiments related to the olivine compaction experiments considered here (Connolly et al., 2009). Equation 23 is integrated numerically by the Lax-Wendroff method. An implicit assumption of the hydraulically-limited model is that the solid matrix is inviscid, the initial height of the sedimentary column for the results depicted here, $10\delta_0$ (Figure 3g), was chosen such that a hydraulically-limited regime would be expected to develop in a column composed of a matrix with finite viscosity (McKenzie, 1984). This regime is characterized by an interval of transient compaction, the top of which, that is, the compaction front, propagates upward from the base of the sedimentary column with velocity $v_{\phi_{\mathrm{sed}}}$ given by Equation 24 at $\phi = \phi_{\mathrm{sed}}$. The transient compaction supplies the fluid flux necessary to maintain, non-compacting, fluidized conditions in the remainder of the column, $q_{\mathrm{f},\phi=\phi_{\mathrm{sed}}}$, the top of which must advect downward with velocity $v_{\mathrm{top}} = -q_{\mathrm{f},\phi=\phi_{\mathrm{sed}}}$ to satisfy mass conservation. Thus, for $n = 3$ and $b = 1$, the compaction front reaches the top of the sedimentary column at time

$$t_{2/3} = \frac{h_0\phi_{\mathrm{sed}}}{q_{\mathrm{f},\phi=\phi_{\mathrm{sed}}}\left(3 - 2\phi_{\mathrm{sed}}\right)} \tag{25}$$

at which the average porosity of the column is $\frac{2}{3}\phi_{\mathrm{sed}}$. Thereafter the porosity at the top of the column decreases with time and compaction slows. Because of this complexity at $t > t_{2/3}$, we suggest $t_{2/3}$ as the characteristic time for hydraulically-limited compaction (i.e., $h_0 > \delta_0$), analogous to the half-times for rheologically-limited compaction. As average porosities in the centrifuge experiments generally exceed plausible values for $\frac{2}{3}\phi_{\mathrm{sed}}$, it is unlikely that the $t_{2/3}$ transition during hydraulically-limited compaction explains the compaction observed at the top of the experimentally generated columns.

Matrix permeability and viscosity are, by far, the most uncertain properties governing viscous compaction. In the hydraulically- and rheologically-limited regimes compaction is governed solely by either the matrix permeability or the matrix viscosity. Our formulations formalize this separation and are approximations that are expected to fail in the limit $\phi \to 0$. The quality of these approximations hinges on the viscous compaction length (McKenzie, 1984), which depends on both matrix permeability and viscosity and is not known a priori for the centrifuge experiments. In particular, during hydraulically-limited compaction, sensu lato, finite matrix viscosity would result in a finite transient porosity at the base of the sedimentary column. Regardless of this shortcoming, hydraulically-limited compaction will generate a convex profile or become unstable with respect to an intermediate regime in which compaction is accomplished by porosity waves (Connolly & Podladchikov, 2000; McKenzie, 1987). As neither scenario is consistent with the observed profiles, which in the case of the olivine experiments are arguably convex, we conclude that the experiments are best interpreted in light of rheologically-limited compaction. Among the three rheologically-limited models, the curvature of the Linear-Weakening and Dislocation profiles is inconsistent with the olivine profiles. This inconsistency does not discriminate deformation mechanism, rather it reflects the inadequacy of the simplified porosity dependence of the matrix shear viscosity assumed for these models, that is, $f_\eta = 1 - \phi$. Indeed, if this porosity dependence is replaced by the weakest plausible porosity dependence for the matrix shear viscosity (Equation 6 with $n_\sigma = 1$) the resulting profiles in both cases are convex for the conditions illustrated in Figure 3. However, as the experimental observations suggest that the deformation mechanism is, in fact, grain-boundary diffusion-controlled creep, we adopt the Diffusion model as the basis for inferring bulk viscosities from the centrifuge experiments. In the limit $h_0 \to \delta_0$, Equation 9 overestimates the effective pressure, thus, if otherwise correct, our analysis provides an upper limit on the bulk viscosity.

5. Analysis of the Centrifuge Experiments

The challenge posed by the centrifuge experiments is that the compaction profiles record the time-integrated viscosity of the samples from an initial condition that is not observed. To address this issue we exploit that at the base of the sedimentary column the $1 - \phi(z,t)$ integrand in Equation 10 can be replaced by $1 - \phi_{\mathrm{avg}}(t)$, where ϕ_{avg} is the average porosity of the column, and, observing that, for 1-dimensional compaction, conservation of solid mass requires that the product $c_\phi = h(t)\left(1 - \phi_{\mathrm{avg}}(t)\right)$ is constant, obtain

$$\frac{D\phi_{\mathrm{base}}}{Dt} = \frac{(1-\phi)}{\eta_{\mathrm{s}} f_\eta \left(c_\xi f_\xi + \frac{4}{3}\right)} c_\phi \Delta\rho a. \tag{26}$$

As the matrix velocity is zero at the base of the sedimentary column, the material derivative in Equation 26 can be replaced by the partial derivative and, taking $f_\xi = 1$, $c_\xi = \frac{5}{3}$, and $f_\eta = f_\eta^{\mathrm{dif}}$ as appropriate for diffusion creep, the result rearranged to an ordinary differential

$$\frac{f_\eta^{\mathrm{dif}}}{(1-\phi_{\mathrm{base}})} \mathrm{d}\phi_{\mathrm{base}} = \frac{c_\phi \Delta\rho a}{3\eta_{\mathrm{s}}} \mathrm{d}, \tag{27}$$

which integrates from the initial time (0) and porosity (ϕ_{sed}) to

$$\begin{aligned} \frac{4\left[\operatorname{artanh}\left(\sqrt{\phi_{\mathrm{sed}}}\right) - \operatorname{artanh}\left(\sqrt{\phi_{\mathrm{base}}}\right) + \sqrt{\phi_{\mathrm{base}}}\right]}{\sqrt{\phi_{\mathrm{sed}}}} + \ln\left(\frac{1-\phi_{\mathrm{sed}}}{1-\phi_{\mathrm{base}}}\right)\left(1 + \frac{1}{\phi_{\mathrm{sed}}}\right) - \frac{\phi_{\mathrm{base}}}{\phi_{\mathrm{sed}}} - 3 \\ = \frac{c_\phi \Delta\rho a}{3\eta_{\mathrm{s}}} t. \end{aligned} \tag{28}$$

To regularize for temperature (T) and grain size, η_{s} is expressed as

Table 2

Summary of Conditions, Data, and Results for the Centrifuge Experiments

Material/experiment	T, K	p, GPa	$-a$, m/s^2	t_{expt}[a], h	h_{expt}[a], μm	ϕ_{avg}	ϕ_{base}	ϕ_{top}	d, μm	$\Delta\rho$, kg/m^3	η_f, Pa s
Olivine, $\phi_{\mathrm{sus}} = 0.652 \pm 0.006$											
ZOB9	1,553	1	2,000	1	700[b]	0.535	0.491	0.578	13.1	420	17
ZOB6	1,553	0.8	2,000	3	625	0.553	0.488	0.618	13.3	420	17
ZOB1	1,553	1.1	4,000	6	450	0.499	0.418	0.580	14.4	420	17
ZOB11	1,553	1	15,000	1.8	620[c]	0.383	0.339	0.427	11.0	420	17
ZOB5	1,553	0.9	7,000	10	675[b]	0.426	0.312	0.539	14.7	420	17
ZOB10	1,553	1	15,000	4.7	463[c]	0.407[b]	0.346	0.474	12.3	420	17
ZOB4	1,553	0.9	4,000	50	560	0.355[b]	0.275	0.433	18.6	420	17
Chromite, $\phi_{\mathrm{sus}} = 0.600 \pm 0.004$											
SM21	1,573	0.5	5,000	6	1,360[c]	0.456	0.441	0.470	11.1	1,880	25.7
SM30	1,573	0.5	7,000	10	1,360[c]	0.440	0.417	0.463	12.0	1,880	25.7
SM17	1,573	0.5	10,000	9	1,420[c]	0.410	0.400	0.421	12.2	1,880	25.7
SM18	1,573	0.5	12,000	10	1,440[c]	0.451	0.427	0.475	11.5	1,880	25.7
SM16	1,573	0.5	15,000	10	1,420[c]	0.414[b]	0.384	0.445	11.3	1,880	25.7
SM29	1,573	0.5	2,000	10	1,470	0.474	0.459	0.489	11.0	1,880	25.7
SM25	1,623	0.5	10,000	10	1,124	0.391	0.380	0.402	12.2	1,880	25.7
SM31	1,673	0.5	10,000	10	1,240	0.399	0.373	0.426	11.4	1,880	25.7
Plagioclase, $\phi_{\mathrm{sus}} = 0.745 \pm 0.006$											
GXZ54	1,498	0.5	10,000	5	2,502[b]	0.635[b]	0.590	0.680	33	11	45
GXZ61	1,523	1	−10,000	5	2,474[b]	0.630[b]	0.575	0.686	33	−37	26
GXZ51	1,498	0.5	−10,000	10	3,105[b]	0.658[b]	0.608	0.708	33	−20	37
GXZ137	1,140	0.5	−10,000	24	3,116[b]	0.550[b]	0.514	0.585	33	−283	80

[a] The subscript expt is used when ambiguity may arise to indicate values at the end of the centrifuging stage of the experiments. [b] Remeasured. [c] Sum of reported virtual segment thicknesses.

$$\eta_s = c_\eta d^m \exp\left(\frac{Q}{\mathrm{R}}\frac{T_0 - T}{T\,T_0}\right) \tag{29}$$

where the grain size exponent $m = 3$, as is characteristic of grain-boundary diffusion-controlled creep, Q is the activation energy (Table 3), R the gas constant, and T_0 an arbitrary reference temperature, set to 1,553 K so as to minimize the differences in the values of viscous coefficient c_η inferred from the 3 sets of experiments due to temperature. Substituting $c_\phi = h_{\mathrm{expt}}\left(1 - \phi_{\mathrm{avg,expt}}\right)$ and Equation 29 into Equation 28, the result is rearranged to express c_η as function of the observed experimental parameters (Table 2) and the unknown sedimentary porosity

$$c_\eta = -\frac{h_{\mathrm{expt}}\left(1 - \phi_{\mathrm{avg,expt}}\right)\Delta\rho a t_{\mathrm{expt}}}{3 f\left(\phi_{\mathrm{base,expt}}, \phi_{\mathrm{sed}}\right) d^m \exp\left(\frac{Q}{\mathrm{R}}\frac{T_0 - T}{T\,T_0}\right)} \tag{30}$$

where $f(\phi_{\mathrm{base,expt}}, \phi_{\mathrm{sed}})$ represents the left-hand side of Equation 28. To estimate ϕ_{sed}, the mean square error on $\log_{10}(c_\eta)$ was minimized as a function of ϕ_{sed} for each set of experiments. The mean $\log_{10}(c_\eta)$ at the optimized value of ϕ_{sed} was then taken as representative of the solid material (Table 3). To illustrate fitting error, $\log_{10}\left(c_\eta f_\eta^{\mathrm{dif}}\right)$ was computed for the individual experiments (blue filled circles, Figure 5) using the optimized value ϕ_{sed} and is compared to $\log_{10}\left(c_\eta f_\eta^{\mathrm{dif}}\right)$ computed with the mean value of $\log_{10}\left(c_\eta\right)$ (heavy blue curves, Figure 5). The variation in sedimentary porosities among the centrifuge experiments (Table 3) is consistent with the expectation that higher packing densities are achieved with more equant grain shapes. To test whether the

Table 3
Optimized Parameters and Intermediate Model Results for the Centrifuge Experiments

Material/experiment	ϕ_{avg}/ϕ_{sed}[a]	c_η[b], Pa s/m^3	δ_{base}/h_{expt}[c]	t_{sed}/t_{expt}[d]	t_{hyd}/t_{expt}[e]	ϕ_{hyd}/ϕ_{sed}[f]
Olivine: $\phi_{sed} = 0.584 \pm 0.022$ $c_\eta = 10^{23.69 \pm 0.11}$ Pa s/m^3 $Q = 335$ kJ/mol[h]						
ZOB9	0.92	$10^{23.53}$	2.0	0.237	0.99	0.93
ZOB6	0.95	$10^{23.88}$	3.6	0.063	0.29	0.96
ZOB1	0.85	$10^{23.59}$	5.9	0.012	0.05	0.97
ZOB11	0.66	$10^{23.72}$	2.7	0.040	0.12	0.90
ZOB5	0.73	$10^{23.64}$	4.6	0.008	0.03	0.95
ZOB10	0.70	$10^{23.89}$	5.8	0.008	0.03	0.96
ZOB4	0.61	$10^{23.60}$	8.8	0.001	0.01	0.97
Chromite: $\phi_{sed} = 0.511 \pm 0.031$ $c_\eta = 10^{25.93 \pm 0.28}$ Pa s/m^3 $Q = 520$ kJ/mol[h]						
SM21	0.89	$10^{25.82}$	4.3	0.086	0.32	0.97
SM30	0.86	$10^{25.72}$	5.6	0.033	0.12	0.97
SM17	0.80	$10^{25.64}$	6.5	0.030	0.10	0.97
SM18	0.88	$10^{26.17}$	7.5	0.022	0.08	0.98
SM16	0.81	$10^{25.78}$	5.9	0.020	0.07	0.97
SM29	0.93	$10^{26.07}$	4.1	0.132	0.51	0.98
SM25	0.77	$10^{25.91}$	5.8	0.022	0.07	0.97
SM31	0.78	$10^{26.46}$	4.8	0.027	0.09	0.96
Plagioclase: $\phi_{sed} = 0.656 \pm 0.072$ $c_\eta = 10^{23.48 \pm 0.85}$ Pa s/m^3 $Q = 153$ kJ/mol[h]						
GXZ54	0.97	$10^{23.87}$	1.9	0.665	2.06	0.95
GXZ61	0.96	$10^{23.22}$	4.0	0.116	0.36	0.97
GXZ51	1.00	$10^{23.91}$	4.3	0.163	0.57	0.98
GXZ137	0.84	$10^{23.80}$	8.0	0.018	0.05	0.98

[a] A measure of the extent of compaction, ϕ_{avg} is the value reported as $\phi_{avg,expt}$ in Table 2. [b] Values used for calculating δ_{base}, t_{hyd}, and ϕ_{hyd}. [c] The local viscous compaction length at the base of the compacted column. [d] t_{sed} is the estimated duration of sedimentation (Equation A4). [e] t_{hyd} is the estimated duration of the putative initial hydraulically-limited stage of compaction (Equation A5). [f] ϕ_{hyd} is the average porosity of the column at t_{hyd} Equation A7. [g] Indicated uncertainties are the standard error. [h] Activation energies for olivine, chromite, and plagioclase are, respectively, from Hirth and Kohlstedt (2003), Suzuki et al. (2008), and Rybacki and Dresen (2004).

resolution of the experiments alone was adequate to distinguish deformation mechanism, f_η^{dif} was replaced by f_η^{dis} (Equation 6) in Equation 27 and the analysis of the olivine experiments repeated for half-integral increments of n_σ over the interval $\left[\frac{1}{2}, \frac{7}{2}\right]$. The best fit was obtained for $n_\sigma = 2$, which is numerically identical to the porosity dependence of f_η^{dif}, however the differences in fit quality were not statistically significant.

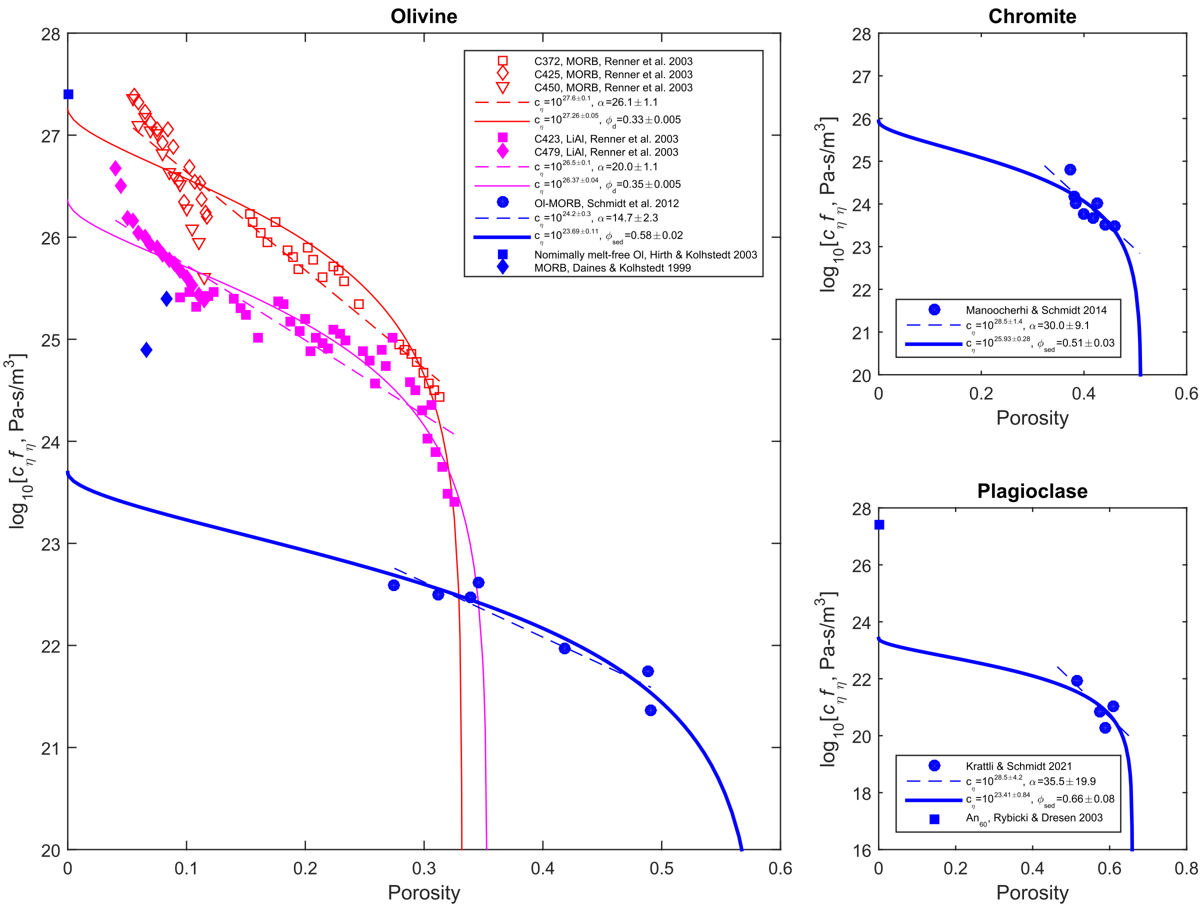

Figure 5. Regression models and data for $\log(c_\eta f_\eta)$ relevant to the centrifuge experiments and, in the case of olivine, to the experiments of Renner et al. (2003), $\log(c_\eta f_\eta)$ is numerically equivalent to the log of the matrix shear viscosity at unit grain size (1 m). For the centrifuge experiments, the circular blue points are computed from Equation 30 for the individual experiments using the value of ϕ_{sed} obtained by optimizing the entire set of experiments on each material. For the Renner et al. (2003) experiments, the data points are computed directly from the individual experiments (i.e., the left-hand side of Equation 31). Solid curves are for f_η as given by Equation 3, dashed curves correspond to the empirical porosity-weakening model (Equation 2) that is often used to represent shear deformation experiments at low porosity (Hirth & Kohlstedt, 2003; Mei et al., 2002). The difference in ϕ_{d}, identified as ϕ_{sed} for the centrifuge experiments, between the Renner et al. (2003) and centrifuge results is expected in that the samples in the former experiments were prepared by isostatic pressing which resulted in a higher grain *CN* than would result from sedimentation. It is argued here that, in the absence of detailed chemical and textural information, during decompaction induced by partial melting or melt infiltration ϕ_{d} is best estimated by the porosity of random close packed spheres, $\phi = 0.36$, which compact to a zero-porosity matrix with an average grain $CN = 13.3$ (Jaeger & Nagel, 1992), whereas the larger values of ϕ_{sed} inferred from the centrifuge experiments are appropriate to sedimentary compaction. Indeed, the values of ϕ_{sed} for olivine and plagioclase match those estimated for natural orthocumulates (Boudreau & Philpotts, 2002; Irvine, 1980; Tegner et al., 2009).

5.1. Back-Calculated Settling Times, Duration of Hydraulically-Limited Compaction, and Compaction Profiles

Two key assumptions of the present analysis are that, relative to the duration of the experiments, the crystals settle rapidly and that the initial hydraulically-limited phase of compaction rapidly increases the compaction-length scale and causes a transition to rheologically-limited compaction. While it is not possible to prove the validity of these assumptions, it is possible to formulate simple models (Appendix A) to test whether the estimated viscosities and sedimentary porosities are consistent with these assumptions. For both the olivine and chromite experiments, computed settling times (t_{sed}) and durations of hydraulically-limited compaction (t_{hyd}) are typically < 10% of the duration of the experiment and the reduction in the average porosity during the hydraulically-limited stage, $\phi_{\text{hyd}}/\phi_{\text{sed}}$, is likewise < 10% (Table 3). More prominent deviations from our analytical assumptions are indicated in the least compacted olivine and chromite experiments. In the plagioclase experiments, large deviations are the rule rather than the exception, with the exception being the most compacted experiment (GXZ137). As discussed in the Appendix, we do not reject the other plagioclase results outright because both t_{sed} and t_{hyd} are inversely proportional to $|\Delta\rho|$, which in the case of the plagioclase experiments is subject to large relative

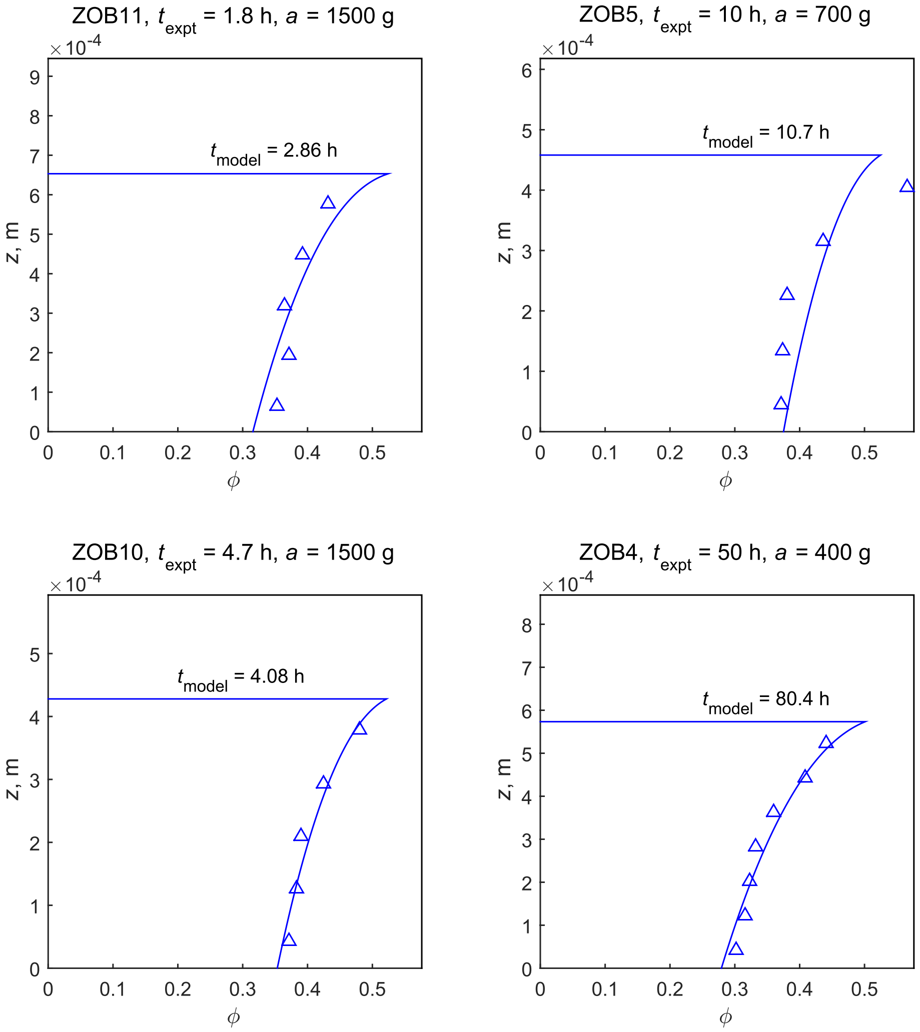

Figure 6. Porosity profiles obtained by numerically integrating the governing equation for rheologically-limited compaction (Equation 10) for the four most compacted olivine centrifuge experiments using the optimized viscous coefficient and sedimentary porosity (Table 3). The initial height and porosity of the uncompacted column correspond to the maximum porosity and height represented on the coordinate frame for each profile. Compaction at the top of the column is caused by incrementing the effective pressure by $d(1-\phi)\Delta\rho a/2$, an increment that corresponds to the weight of a porous olivine layer with a thickness of half the experimental grain-size. The measured porosities of the experimental profiles are indicated by triangular symbols. The computed profiles were chosen to match the average porosity of the corresponding experiment. In calculations made without the effective pressure increment (not shown), computed compaction half-times increase by roughly 10% and the surface porosity (ϕ_{top}) remains uncompacted but there is no significant impact on the quality of the match with the observed profiles.

error (Krattli & Schmidt, 2021). The model for duration of hydraulically-limited compaction estimates t_{hyd} as the time at which $\delta(\phi_{avg}(t_{hyd})) = h(t_{hyd})$, thus it follows that $\delta(\phi_{avg}(t)) > h(t)$ for $t > t_{hyd}$. An alternative, more optimistic, assessment of the degree to which experimental conditions tended toward the rheologically-limited regime is to compute δ/h from ϕ_{base} (Table 3). This measure places the experiments within an order of magnitude of the $h/\delta = 1$ condition at which the influence of matrix permeability and viscosity are comparable. As noted earlier, deviations from our analytical assumptions are likely to lead us to overestimate both the matrix viscosity and h/δ.

To further demonstrate the consistency of the regression results, rheologically-limited compaction profiles were computed from Equation 10 so as to match $\phi_{avg,expt}$ for the four most compacted, and therefore presumably best resolved, olivine experiments (Figure 6) under the assumption that the effective pressure in the top-most layer of grains is $d(1-\phi)\Delta\rho a/2$. The agreement between the observed and predicted profiles is remarkable given that c_η was estimated only from $\phi_{\mathrm{base,expt}}$, this success is an argument for the validity of the porosity dependence (Equation 3) advocated on the basis of analytical and numerical models (Rudge, 2018; Takei & Holtzman, 2009a). The deviation between experimental and model times required to reproduce $\phi_{\mathrm{avg,expt}}$ is within a factor of two.

6. Discussion

The physical significance of the property η_s identified here as the shear viscosity in the limit $\phi \to 0$ is the subject of a controversy that originates from the experimental observation that the shear viscosity of truly melt-free olivine aggregates drops by about a factor of 20 with the introduction of a minute ($\phi \approx 10^{-4}$) amount of melt (Faul & Jackson, 2007). Takei and Holtzman (2009b) attribute this drop to a change from melt- to grain-boundary diffusion-limited mass transport. The transition would be sensitive to grain size and is expected, on the basis of Faul & Jackson's observations, to occur at melt fractions below the amounts of melt normally present in nominally melt-free experiments. Takei and Holtzman (2009b) predict that at still lower melt fractions the bulk strain rate becomes limited by reaction kinetics, a transition that would affect both the porosity- and grain-size dependence of the bulk viscosity (Raj, 1982; Shimizu, 1995). There are reasons to question the relevance of these transitions (Rudge, 2018; Takei, 2017) but there is no doubt that if they occur, then they would have important consequences for melt extraction and transport at porosities below $\sim 10^{-3}$ (Holtzman, 2016). Because our results are derived from experiments at higher porosities and extrapolated to zero porosity using a relation derived for grain-boundary diffusion-limited creep, η_s compares to the shear viscosity of nominally melt-free experiments but may not be identical to viscosity of the truly melt-free matrix. On this basis, we compare our results to previous experimental studies.

6.1. Comparison With Previous Experimental Studies

Daines and Kohlstedt (1993) and Renner et al. (2003) investigated the compaction of partially molten olivine aggregates at porosities intermediate between those of shear deformation experiments (e.g., Hirth & Kohlstedt, 1995; Mei et al., 2002) and the sedimentary porosities considered here. Daines and Kohlstedt (1993) treated self-induced compaction and, as for the centrifuge experiments, the interpretation of their experiments is complicated by the necessity of assuming and integrating a compaction model. Taken at face value, their results (Figure 5) indicate viscosities more than an order of magnitude greater than those inferred here but do not constrain the porosity dependence of the viscosity. Renner et al. (2003) measured instantaneous compaction rates of samples containing either MORB (i.e., basaltic) or Li-Al-silicate melt as a function of externally-controlled melt pressure at various confining pressures; thus, the bulk viscosity and its porosity dependence were, essentially, directly measured. The patterns for individual samples, particularly at low porosity suggest the possibility of mechanical interference from the deformation apparatus, as discussed by Renner et al. (2003); discounting this possibility, the samples have been grouped according to melt chemistry and fit to the regression model

$$\left[\frac{1}{1-\phi}\frac{\mathrm{D}(1-\phi)}{\mathrm{D}t}\frac{d^m c_\xi^{\mathrm{dif}}}{p_\mathrm{e}}\exp\left(\frac{Q^{\mathrm{dif}}}{\mathrm{R}}\frac{T-T_0}{TT_0}\right)\right]^{-1} = c_\eta\left(1-\sqrt{\phi/\phi_\mathrm{d}}\right)^2 \qquad (31)$$

for c_η and ϕ_d (Figure 5), where the response variable on the left-hand side is obtained by substituting Equations 1, 3, and 29 into Equation 8 and collecting known and observed parameters. Given that the MORB and Li-Al-silicate melts have comparable wetting properties, the order of magnitude difference in c_η suggests a chemical effect; however the porosity dependence of both groups is well-described by f_η^{dif} (Equation 3) and, in the case of the MORB liquid, extrapolates within error to the value of c_η for the synthesis model for diffusion creep in olivine constructed by Hirth and Kohlstedt (2003). In contrast, c_η for the olivine centrifuge experiments is four orders of magnitude below the synthesis model, a discrepancy that is beyond estimated experimental error. We speculate that this discrepancy may be related to the difference in the effective pressures for the Renner (p_e = 5–50 MPa) and the centrifuge experiments (p_e = 0.5–4 kPa); however, deviation from linear viscous behavior, as has been reported for diffusion creep in melt-free olivine-aggregates (Faul & Jackson, 2007), would be more likely to

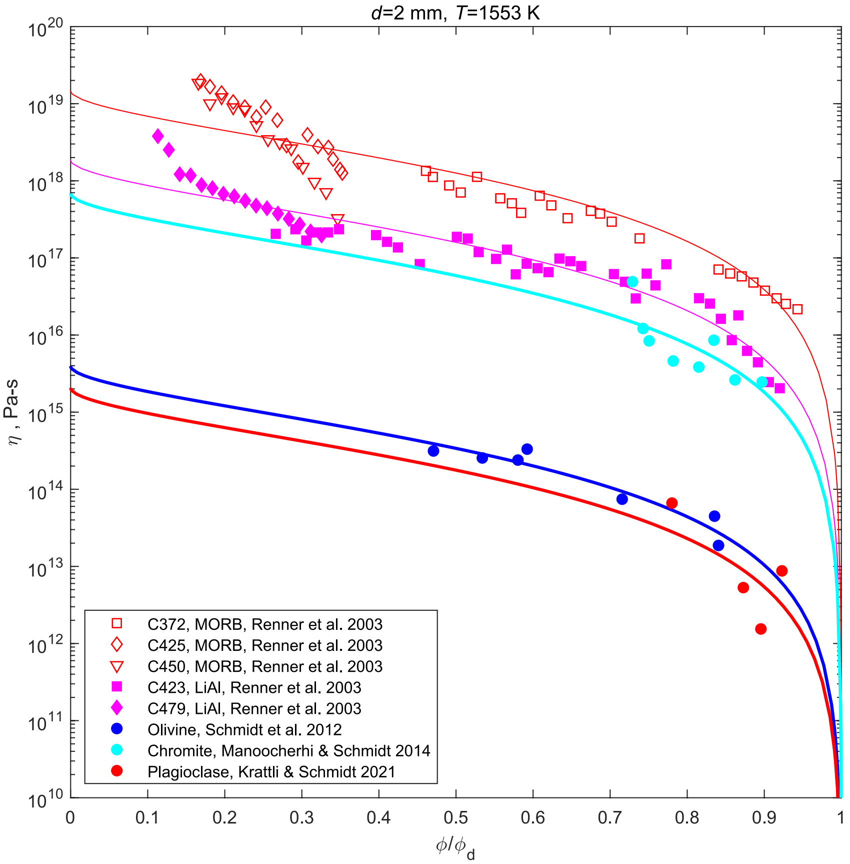

Figure 7. Matrix shear viscosities as a function of the relative porosity ϕ/ϕ_{d} for the centrifuge experiments and the experiments of Renner et al. (2003). The viscosities have been regularized to a common grain size (2 mm) and temperature (1,553 K).

exacerbate the discrepancy than to explain it. Below we note that the viscosity derived from the centrifuge experiments is consistent with estimates derived from geophysical inversions.

Comparison of the porosity-weakening effect is more felicitous in that in both the Renner et al. (2003) and centrifuge experiments (Figure 5) the effect is well-represented by f_{η}^{dif}, albeit for significantly different values of ϕ_{d}. The differences in ϕ_{d} are not unexpected (Vigneresse et al., 1996). In the case of the Renner experiments the differences are consistent with the variation in wetting properties between the MORB and Li-Al-silicate liquids (Rudge, 2018; Takei & Holtzman, 2009a) and reflect the high *CN* obtained by hot-isostatic pressing during sample preparation. The respective values ($\phi_{\mathrm{d}} = 0.34$ and 0.38, Figure 5) bracket the porosity, $\phi = 0.36$, of random close-packed spheres (Jaeger & Nagel, 1992), which we suggest as the best choice for ϕ_{d} in the absence of chemical and textural information. The higher values of ϕ_{sed} for the centrifuge experiments reflect the low *CN* resulting from the sedimentary process. These values are comparable to the porosities of natural orthocumulates (Boudreau & Philpotts, 2002; Irvine, 1980; Tegner et al., 2009). There is little overlap between the absolute porosities of the centrifuge experiments and those of Renner et al. (2003). However, to the extent that the differences in ϕ_{d} reflect process dependent grain *CN*, it is more meaningful to compare the experimental results as a function of the relative porosity ϕ/ϕ_{d}. In terms of ϕ/ϕ_{d}, there is substantial overlap among the experiments (Figure 7) and the trends suggest that it is improbable that the discrepancies in c_{η} inferred from each set of experiments can be attributed to the use of f_{η}^{dif} to extrapolate measurements made at finite porosity to zero porosity.

There are no experimental compaction studies comparable to the plagioclase and chromite centrifuge experiments and only one experimental study of the diffusion creep viscosity of partially molten andesine plagioclase (A. Diamov cited by Rybacki & Dresen, 2004). As in the case of olivine, extrapolation of the plagioclase fit to zero porosity yields a shear viscosity that is four orders of magnitude below this earlier work (Figure 5).

6.2. Dislocation Versus Diffusion Creep

Both the dislocation and diffusion creep regimes are readily accessible experimentally in partially molten aggregates of olivine and plagioclase but extrapolation of constitutive relations to natural conditions is fraught with uncertainty. To make a first order assessment of the viability of diffusion creep in natural settings we consider two scenarios: isostatic and shear-enhanced compaction. The isostatic case recognizes the true, but commonly neglected, non-linear stress dependence of the dislocation creep regime; whereas the shear-enhanced case defines the regime in which effectively linear-viscous compaction might occur in non-linear viscous media subject to macroscopic deviatoric stress. In the isostatic scenario the boundary between the diffusion and dislocation creep regimes is defined by the effective pressure at which the bulk strain rate by either mechanism is equal, where for diffusion creep

$$\frac{1}{1-\phi}\frac{\mathrm{D}(1-\phi)}{\mathrm{D}t} = \frac{p_\mathrm{e}}{c_\eta d^m c_\xi^\mathrm{dif} f_\eta^\mathrm{dif}} \exp\left(\frac{Q^\mathrm{dif}}{\mathrm{R}}\frac{T-T_0}{TT_0}\right) \tag{32}$$

with parameters from Table 3, and for dislocation creep

$$\frac{1}{1-\phi}\frac{\mathrm{D}(1-\phi)}{\mathrm{D}t} = \frac{p_\mathrm{e}\left|p_\mathrm{e}^{n_\sigma-1}\right|}{c_\xi^\mathrm{dis} f_\xi^\mathrm{dis} f_\eta^\mathrm{dis}} A \exp\left(-\frac{Q^\mathrm{dis}}{\mathrm{R}T}\right) \tag{33}$$

with $n_\sigma = 3.5$, $A = 1.1{\cdot}10^{-16}$ Pa$^{-3.5}$/s, and $Q^\mathrm{dis} = 530$ kJ/mol (Hirth & Kohlstedt, 2003). In this scenario, for temperatures and grain sizes chosen to represent the conditions of melt transport and cumulate sedimentation (Table 4), diffusion creep is dominant at small porosity for all plausible effective pressures (Figure 8); to put these in perspective, in a well-connected (i.e., $h < \delta$) olivine basalt-liquid column $p_\mathrm{e} \sim h\Delta\rho g$, thus a column height of ∼ 25 km is required to generate an effective pressure of ∼ 1 MPa. A complicating, but likely robust, feature of this formulation is that for $n_\sigma > 2$, the porosity-weakening of the dislocation creep rheology is stronger than it is for diffusion creep. Thus, dislocation creep must become the dominant mechanism in the limit $\phi \to \phi_\mathrm{d}$. This effect may be relevant to natural cumulates (McKenzie, 2011), but for the ∼ 10^{-5} m grain sizes of the centrifuge experiments the effect would not be observable due to the rapid relative strengthening of the dislocation creep rheology during compaction. For example, at such grain sizes, our parameterization places the transition to a dislocation creep dominated regime for $\phi/\phi_\mathrm{d} = 0.999$ at $p_\mathrm{e} \sim 10$ MPa, at least three orders of magnitude greater than the effective pressures realized in the centrifuge experiments. For the shear-enhanced scenario, the boundary between the diffusion and dislocation creep regimes is drawn by equating bulk strain rate for diffusion creep (Equation 32) with

Table 4
Bulk Viscosity From the Centrifuging Experiments and Scales Extrapolated to Conditions Relevant to Natural Igneous Sedimentation and Melt-Flow in Partially Molten Rocks

Cumulate compaction:								Diffusion			Linear-Weakening			Dislocation		
	T, K	d, mm	$\Delta\rho$, kg/m^3	η_f, Pa s	h, m	ϕ_sed	ϕ_0	ξ_0^dif, Pa s	δ_0^dif, m	$t_{1/2}^\mathrm{dif}$, y	ξ_0^lin, Pa s	δ_0^lin, m	$t_{1/2}^\mathrm{lin}$, y	ξ_0^dis, Pa s	δ_0^dis, m	$t_{1/2}^\mathrm{dis}$, y
Olivine	1,553	4	420	50	30	0.58	0.29	4×10^{15}	2×10^{3}	2×10^{3}	4×10^{16}	6×10^{3}	4×10^{4}	6×10^{16}	7×10^{3}	5×10^{4}
Chromite	1,553	1	1,880	50	1	0.51	0.26	1×10^{16}	7×10^{2}	2×10^{4}	1×10^{17}	2×10^{3}	5×10^{5}	2×10^{17}	3×10^{3}	7×10^{5}
Plagioclase	1,553	4	10	50	30	0.66	0.33	3×10^{15}	2×10^{3}	7×10^{4}	2×10^{16}	6×10^{3}	2×10^{6}	3×10^{16}	7×10^{3}	2×10^{6}

Melt flow in partially molten rock:							Diffusion			Linear-Weakening			Dislocation		
	T, K	d, mm	$\Delta\rho$, kg/m^3	η_f, Pa s	ϕ_d	ϕ_0	ξ_0^dif, Pa s	δ_0^dif, m	τ_0^dif, y	ξ_0^lin, Pa s	δ_0^lin, m	τ_0^lin, y	ξ_0^dis, Pa s	δ_0^dis, m	τ_0^dis, y
Olivine	1,373	2	420	100	0.36	10^{-2}	1×10^{17}	2×10^{1}	8×10^{2}	2×10^{17}	3×10^{1}	1×10^{3}	9×10^{18}	1×10^{2}	5×10^{3}
						10^{-4}	2×10^{17}	3×10^{-2}	1×10^{4}	2×10^{17}	3×10^{-2}	1×10^{4}	1×10^{21}	2×10^{0}	5×10^{5}
Plagioclase	1,373	2	200	100	0.36	10^{-2}	1×10^{16}	7×10^{0}	6×10^{2}	2×10^{16}	8×10^{0}	6×10^{2}	8×10^{17}	4×10^{1}	3×10^{3}
						10^{-4}	2×10^{16}	8×10^{-3}	6×10^{3}	2×10^{16}	8×10^{-3}	6×10^{3}	7×10^{19}	4×10^{-1}	3×10^{5}

Note. Linear-Weakening and Dislocation refer to the porosity dependence of those models and not the value of c_η used to compute η_s, which for all three cases derives from the centrifuge experiments (Table 3).

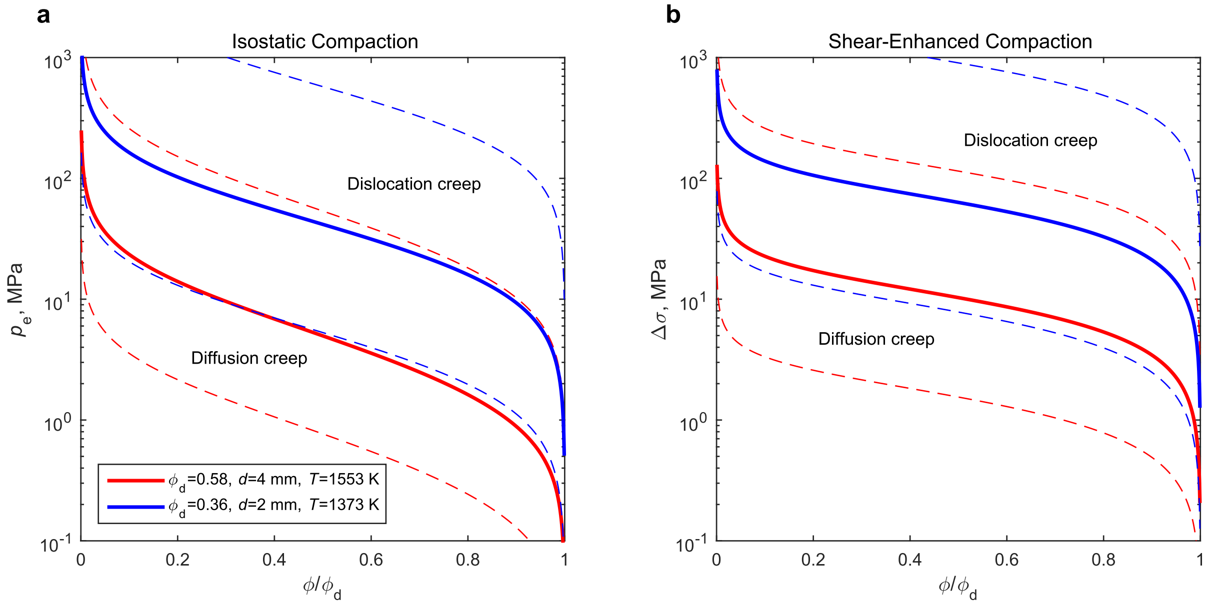

Figure 8. Boundary between the diffusion and dislocation creep regimes for olivine as a function of stress and relative porosity computed using the diffusion creep parameters derived from the centrifuge experiments and the synthesis parameterization for dislocation creep (Hirth & Kohlstedt, 2003). (a) Effective pressure at which the compaction rate by diffusion creep and truly non-linear dislocation creep are equivalent (continuous curves). (b) Magnitude of the deviatoric stress at which the effective viscosity for the dislocation creep rheology is equal to the diffusion creep viscosity, at stresses in excess of this threshold (continuous curves) the linear Dislocation model may be justified. Red and blue boundaries are computed for parameters chosen to represent, respectively, igneous sedimentation and asthenospheric melt transport (Table 4). Dashed curves indicate the error on the boundaries attributable to the estimated error on the dislocation creep stress exponent ($n_\sigma = 3.5 \pm 0.3$) and the diffusion creep viscous coefficient ($c_\eta^{\text{dif}} = 10^{23.7\pm0.11}$ Pa s/m^3).

$$\frac{1}{1-\phi}\frac{\mathrm{D}(1-\phi)}{\mathrm{D}t} = \frac{p_\mathrm{e}}{c_\xi^{\text{dis}} f_\xi^{\text{dis}} \eta^{\text{dis}}} \tag{34}$$

where c_ξ^{dis} and f_ξ^{dis} are computed from Equations 4 and 5 with $n_\sigma = 1$, and the effective shear viscosity of the matrix for the dislocation creep regime is

$$\eta^{\text{dis}} = f_\eta^{\text{dis}} \left[|\Delta\sigma|^{n_\sigma - 1} A \exp\left(-Q^{\text{dis}}/\mathrm{R}/T\right)\right]^{-1}, \tag{35}$$

with parameters as in Equation 33 and $\Delta\sigma$ is taken as a proxy for the macroscopic deviatoric stress. As both Equations 32 and 34 are linear in p_e, equivalence of the bulk strain rates is only a function of the deviatoric stress (Figure 8a). The logic of this construction being that, at $\Delta\sigma >> p_\mathrm{e}$, $(|\Delta\sigma| + |p_\mathrm{e}|)^{n_\sigma - 1} \approx |\Delta\sigma|^{n_\sigma - 1}$ and η^{dis} is essentially independent of p_e so that compaction occurs by the non-linear dislocation creep mechanism with an apparently linear viscous response to p_e. Thus, the necessary conditions for this regime are that $\Delta\sigma$ exceeds the value predicted by equating the strain rates given by Equations 32 and 34 and that $\Delta\sigma >> p_\mathrm{e}$. As igneous sediments are unlikely to sustain large non-hydrostatic stresses, if the shear-enhanced scenario has relevance to natural systems, then it as at the low porosities characteristic of melt transport (solid blue curve, Figure 8b) where the shear-enhanced scenario parameterization implies deviatoric stresses in excess of ∼ 100 MPa are necessary to generate a linear-viscous compaction rheology from solid grains that deform by dislocation creep. Our intention is not to advocate this scenario, rather it is to demonstrate that it is difficult to justify the $\xi \propto 1/\phi$ assumption, which remains common in macroscopic compaction models (e.g., Dohmen et al., 2019; Jackson et al., 2018), in that the only geologically relevant rheology from which it can be derived is dislocation creep.

The p_e and $\Delta\sigma$ conditions in Figure 8 are shifted by a factor of two in favor of diffusion creep by a 100 K reduction in temperature, by a factor of eight in favor of dislocation creep by a doubling of grain size, and are weakly dependent on ϕ_d. These effects are dwarfed by inter-laboratory discrepancy of four-orders of magnitude in c_η, such that the values for c_η derived from earlier work essentially exclude any role for diffusion creep in partially molten mantle rocks.

6.3. Cumulate Compaction

The centrifuge experiments are a direct analogy to the compaction of an igneous cumulate layer that has formed by rapid sedimentation. The present work has demonstrated two effects that have profound consequences for cumulate compaction: the calibration of the diffusion creep rheology; and the non-linear porosity dependence of the shear viscosity. The time required for a self-compacting layer to halve its porosity, that is, $t_{1/2}$, is proportional to $\delta_0\tau_0$ (Equations 13–15) and therefore proportional to viscosity. Thus, for olivine and plagioclase, the calibration effect enhances compaction rates by four orders of magnitude compared to those that would be estimated from earlier experimental work. Despite this enhancement, for typical grain sizes and layer thicknesses (Table 4; Irvine, 1975; Mondal & Mathez, 2007; Tegner et al., 2009), olivine is the only matrix mineralogy for which the characteristic time, $O(10^3)$y, is short compared to the time-scale of cumulate systems. The longer $O(10^4–10^5)$y characteristic times for plagioclase and chromite layers suggest that viscous compaction is effective in such layers only if they are loaded by additional sedimentation, which, in the case of plagioclase additionally requires that the layer forms by settling rather than floating. Accounting for the non-linear porosity dependence of diffusion creep increases the efficacy of compaction by a factor of 20–50 (Equations 18 and 19, Table 4) compared to the porosity dependences commonly adopted in cumulate compaction literature mentioned earlier (Section 3). Thus, in combination, the calibration and porosity-weakening effects increase the estimated efficacy of viscous compaction in magmatic sediments by five orders of magnitude. More importantly, strong porosity-weakening leads to more uniform porosity during compaction with the result that in multi-layer cumulates melt expulsion is less likely to become choked off by low-porosity layers and transition to a hydraulically-limited regime at depth (Connolly & Podladchikov, 2000; Shirley, 1986; Sumita et al., 1996).

6.4. Partial Melting and Melt Flow

If the olivine and plagioclase results from the centrifuge experiments are extrapolated to plausible grain-sizes and temperatures for asthenopheric (McKenzie, 1985) and trans-crustal magmatic systems (Sparks et al., 2019), the $O(10^{17})$Pa s viscosities obtained (Table 4) are consistent with the range of shear viscosities ($10^{16}–10^{18}$ Pa s) inferred for these settings from geophysical inversions (Jones & Maclennan, 2005; Marquart et al., 1999; Morgan & Smith, 1992; Selway et al., 2020; Vergnolle et al., 2003; Yamasaki & Kobayashi, 2018). At the low porosities characteristic of compaction-driven flow during partial melting the compaction time and length scales of the Diffusion and Linear-Weakening models converge, while the Dislocation model diverges from the other two (Table 4) due to the assumption that ξ varies as $1/\phi$. As the efficacy of melt expulsion across a partially molten region of given thickness varies inversely with $\delta_0\tau_0$, and thus viscosity, the Dislocation model results in drastically less efficient melt expulsion (Holtzman, 2016). It is broadly accepted that in partially molten rocks melt flow may be accomplished by self-propagating domains of high porosity, that is, porosity waves (Richter & McKenzie, 1984; Scott & Stevenson, 1984). Taking the Linear-Weakening formulation as representative of the low-porosity steady-state porosity-wave solution to the compaction equations, wave velocities are $O(10)v_0$ (Connolly & Podladchikov, 2015), where v_0 is the Darcyian velocity (q_f/ϕ_0, Equation 21) of the melt through the unperturbed matrix. For such velocities, wavelengths are $O(10)\delta_0$, that is, $< O(10)$m. Two implications of these scales are: that in the porosity-wave regime, melt transport is accomplished by numerous, spatially small, albeit potentially large amplitude, waves; and that such short viscous compaction lengths may promote melt transport by magmatic diapirs (Dohmen & Schmeling, 2021). Although small waves would increase the rate of melt expulsion relative to uniform melt flow, and are capable of carrying geochemical signatures (Jordan et al., 2018), they would be indistinguishable from homogeneous flow by geophysical methods except, perhaps, as seismic tremors (Skarbek & Rempel, 2016). Regardless of transport mechanism, geochemical evidence that melts generated at low degrees of partial melting $O(10^{-4})$ beneath mid-ocean ridges reach the surface on a time-scale of $O(10^3)$y (Rubin et al., 2005), are inconsistent with the $O(10^5)$y compaction time-scale (Table 4) that results from the Dislocation model applied to either the centrifuge experiments or the shear viscosities inferred from geophysical inversion.

7. Conclusion

Grain-size sensitive creep is the only geologically relevant mechanism to give rise to the truly linear viscous macroscopic compaction rheology assumed in geodynamic modeling of compaction-driven fluid flow. However, it has long been recognized in rock mechanics (Cooper & Kohlstedt, 1984) that grain-size sensitive creep mechanisms are non-Newtonian on the scale of individual grains and it is this scale that controls the relation between the macroscopic shear and bulk viscosities of a porous rock matrix. Microscopic modeling (Rudge, 2018; Takei & Holtzman, 2009a) has shown that the consequences of this scale-dependence are profound in that in truly Newtonian porous media $\xi \rightarrow \infty$ in the limit $\phi \rightarrow 0$, whereas in the specific case of grain-boundary diffusion-controlled creep, which is generally considered to be the primary deformation mechanism in partially molten rocks, $\xi \propto \eta$ in the same limit. The present work has demonstrated that the porosity-dependence distilled from these microscopic models is consistent with experimental observations in the opposite limit $\phi \rightarrow \phi_{\mathrm{d}}$ and, perhaps more importantly, that the porosity-dependence generally assumed in geodynamic models is inconsistent with these observations. Thus, even in light of the large uncertainties associated with geodynamic models, the microscopic compaction mechanism has significant consequences on model outcomes. From a practical perspective there are currently only three linear viscous mechanisms to choose from: grain-boundary diffusion-controlled creep, Nabarro-Herring creep (Rudge, 2018), and creep by an unspecified Newtonian microscopic mechanism. Given that only grain-boundary diffusion creep is supported by both theory and observation we make the case that it is the most apt choice for generic models of compaction-driven fluid flow. In the small porosity limit, this choice differs little from the formulation originally proposed by McKenzie (1984).

Appendix A: Settling and Hardening Times

During settling from a uniform suspension of non-compacting solid grains conservation of solid mass requires

$$v_{\mathrm{top}}\left(\phi_{\mathrm{sus}}-\phi_{\mathrm{sed}}\right)+v_{\mathrm{settle}}\left(1-\phi_{\mathrm{sus}}\right)=0 \tag{A1}$$

where v_{top} is the velocity of the top of the sedimentary column and v_{settle} is the settling velocity (Figure 1c)

$$v_{\mathrm{settle}}=\frac{d^{2}\Delta\rho a}{18\eta_{\mathrm{f}}}\phi_{\mathrm{sus}}^{s} \tag{A2}$$

where the exponent s is introduced to account for hindered settling at low melt fractions (i.e., $s = 0$ for true Stokes settling). The power-law porosity dependence of Equation A2 has theoretical justification (Richardson & Zaki, 1954) but is sensitive to grain shape. Given that both the Carman-Kozeny porosity-permeability relation and Equation A2 are approximate in that they are based on idealizations and, as noted in the text, must be consistent in the limit $\phi_{\mathrm{sus}} \rightarrow \phi_{\mathrm{sed}}$, we force consistency among Darcy's law (Equation 21), the Carman-Kozeny relation (Equation 22), and Equation A2 by setting $s = n-1 = 2$. This value is slightly below the range, 2.5–5.5, determined experimentally (Tomkins et al., 2005), but the difference is of minor consequence at the large porosities relevant here. Substituting Equation A2 into Equation A1 yields

$$v_{\mathrm{top}}=-\frac{d^{2}\Delta\rho a}{18\eta_{\mathrm{f}}}\phi_{\mathrm{sus}}^{s}\frac{\left(1-\phi_{\mathrm{sus}}\right)}{\left(\phi_{\mathrm{sus}}-\phi_{\mathrm{sed}}\right)}. \tag{A3}$$

Expressing the height of the column when sedimentation ceases, h_0, in terms of the experimentally observed column height and average porosity (Table 2) and the inferred sedimentary porosity (Table 3), the time at which sedimentation ceases is

$$t_{\mathrm{sed}}=-\frac{h_{0}}{v_{\mathrm{top}}}=-h_{\mathrm{expt}}\frac{18\eta_{\mathrm{f}}}{d^{2}\Delta\rho a\phi_{\mathrm{sus}}^{s}}\frac{\left(\phi_{\mathrm{sus}}-\phi_{\mathrm{sed}}\right)\left(1-\phi_{\mathrm{avg,expt}}\right)}{\left(1-\phi_{\mathrm{sus}}\right)\left(1-\phi_{\mathrm{sed}}\right)}. \tag{A4}$$

For hindered Stokes settling, with $s = n-1 = 2$, the settling times computed from Equation A4 (Table 3), using the experimental parameters and the values of ϕ_{sed} deduced from the analysis of the centrifuge experiments, are generally a small fraction of the duration of the experiments and thus reasonably consistent with the instantaneous sedimentation assumption, the ZOB9 olivine and GXZ54 plagioclase experiments being prominent exceptions.

To estimate the duration of the hydraulically-limited compaction phase in the centrifuge experiments it is assumed that the transition to the rheologically-limited regime occurs abruptly when the viscous compaction length-scale becomes comparable to the column height. Such a transition is likely in view of the super-exponential hardening rate resulting from Equation 3 as porosity decreases from ϕ_{sed} (Figure 3). To simulate such a transition, we consider hydraulically-limited compaction of a sedimentary column subject to a constant basal fluid flux, chosen so that the porosity of the column cannot compact below the porosity ϕ_{base}, which serves as a proxy for the porosity of the transition to the rheologically-limited regime. Until the compaction front reaches the top of the column at time t_{hyd}, the velocity of compaction front, v_ϕ, is constant and given by Equation 24. The integral of the divergence of the fluid flux over the length of the column is likewise constant and thus $v_{\mathrm{top}} = -\left(q_{\phi=\phi_{\mathrm{sed}}} - q_{\phi=\phi_{\mathrm{base}}}\right)$ and

$$t_{\mathrm{hyd}} = \frac{h_0}{\left(v_{\phi,\phi=\phi_{\mathrm{sed}}} + q_{\phi=\phi_{\mathrm{sed}}} - q_{\phi=\phi_{\mathrm{base}}}\right)}. \tag{A5}$$

At which time, the height and average porosity of the column are, resprctively,

$$h_{\mathrm{hyd}} = \frac{v_{\phi,\phi=\phi_{\mathrm{sed}}} h_0}{\left(v_{\phi,\phi=\phi_{\mathrm{sed}}} + q_{\phi=\phi_{\mathrm{sed}}} - q_{\phi=\phi_{\mathrm{base}}}\right)} \tag{A6}$$

and

$$\phi_{\mathrm{hyd}} = 1 - \frac{h_0\left(1-\phi_{\mathrm{sed}}\right)}{h_{\mathrm{hyd}}}. \tag{A7}$$

The unknown value of ϕ_{base} is obtained by solving $\delta_{\phi=\phi_{\mathrm{hyd}}} = h_{\mathrm{hyd}}$ numerically, where the initial height is expressed in terms of the experimental observations and the inferred sedimentary porosities and all other parameters are as given in Tables 2 and 3. The short duration of the hydraulically-limited stage of compaction estimated in this manner is, for the most part, consistent with the assumption that most of the compaction during the centrifuge experiments occurs under rheologically-limited conditions. The ZOB9 olivine and GXZ54 plagioclase experiments again being prominent exceptions (Table 3) as our analysis implies that these experiments compacted entirely in the hydraulically-limited regime. The extraordinarily small density contrasts in the plagioclase experiments are the likely culprit re GXZ54, as in some experiments (Krattli & Schmidt, 2021), that were not used here, the drift in confining pressure was sufficient to change the direction of settling. Indeed, the reported density differences lie within the error of the empirical equations of state used to estimate them. Thus, while the direction of settling in the plagioclase experiments unambiguously indicates the sign of the density contrast, the uncertainty in its magnitude is substantial. We do not reject the ZOB9 and GXZ54 results outright because the $\delta_{\phi=\phi_{\mathrm{hyd}}} = h_{\mathrm{hyd}}$ criterion is an order-of-magnitude estimator and because neither experiment significantly influences our results.

Data Availability Statement

Data is available through Schmidt et al. (2012), Manoochehri and Schmidt (2014), and Krattli and Schmidt (2021).

Acknowledgments
We are grateful to an anonymous reviewer and John Rudge for exceptionally diligent and constructive reviews; to Evangelos Moulas and Tobias Keller for discussion that clarified JADC's limited understanding of effective pressure; to Giuliano Kraettli for making a preliminary compilation of the centrifuge experiments; to Sharzad Manoochehri for providing us with data from (Manoochehri & Schmidt, 2014) in digital form; and to Giulio Solferino for making his PhD thesis (Solferino, 2008) publicly available. Open access funding provided by Eidgenossische Technische Hochschule Zurich.

References

Arzt, E., Ashby, M. F., & Easterling, K. E. (1983). Practical applications of hot-isostatic pressing diagrams—4 case studies. *Metallurgical Transactions A: Physical Metallurgy and Materials Science*, *14*(2), 211–221. https://doi.org/10.1007/bf02651618

Bercovici, D., Ricard, Y., & Schubert, G. (2001). A two-phase model for compaction and damage 1. General theory. *Journal of Geophysical Research: Solid Earth*, *106*(B5), 8887–8906. https://doi.org/10.1029/2000jb900430

Birchwood, R. A., & Turcotte, D. L. (1994). A unified approach to geopressuring, low-permeability zone formation, and secondary porosity generation in sedimentary basins. *Journal of Geophysical Research*, *99*(B10), 20051–20058. https://doi.org/10.1029/93jb02388

Boudreau, A., & Philpotts, A. R. (2002). Quantitative modeling of compaction in the Holyoke flood basalt flow, Hartford basin, Connecticut. *Contributions to Mineralogy and Petrology*, *144*(2), 176–184. https://doi.org/10.1007/s00410-002-0391-4

Connolly, J. A. D., & Podladchikov, Y. (2015). An analytical solution for solitary porosity waves: Implications for dynamic permeability and fluidization of nonlinear viscous and viscoplastic rock. *Geofluids*, *15*(1–2), 269–292. https://doi.org/10.1111/gfl.12110

Connolly, J. A. D., & Podladchikov, Y. Y. (2000). Temperature-dependent viscoelastic compaction and compartmentalization in sedimentary basins. *Tectonophysics*, *324*(3), 137–168. https://doi.org/10.1016/s0040-1951(00)00084-6

Connolly, J. A. D., Schmidt, M. W., Solferino, G., & Bagdassarov, N. (2009). Permeability of asthenospheric mantle and melt extraction rates at mid-ocean ridges. *Nature*, *462*(7270), 209–212. https://doi.org/10.1038/nature08517

Cooper, R. F., & Kohlstedt, D. L. (1984). Solution-precipitation enhanced diffusional creep of partially molten olivine-basalt aggregates during hot-pressing. *Tectonophysics*, *107*(3–4), 207–233. https://doi.org/10.1016/0040-1951(84)90252-x

Cooper, R. F., Kohlstedt, D. L., & Chyung, K. (1989). Solution-precipitation enhanced creep in solid-liquid aggregates which display a non-zero dihedral angle. *Acta Metallurgica*, *37*(7), 1759–1771. https://doi.org/10.1016/0001-6160(89)90061-8

Daines, M. J., & Kohlstedt, D. L. (1993). A laboratory study of melt migration. *Philosophical Transactions of the Royal Society of London Series a-Mathematical Physical and Engineering Sciences*, *342*(1663), 43–52. https://doi.org/10.1098/rsta.1993.0003

Dimanov, A., Dresen, G., & Wirth, R. (1998). High-temperature creep of partially molten plagioclase aggregates. *Journal of Geophysical Research: Solid Earth*, *103*(B5), 9651–9664. https://doi.org/10.1029/97jb03742

Dohmen, J., & Schmeling, H. (2021). Magma ascent mechanisms in the transition regime from solitary porosity waves to diapirism. *Solid Earth*, *12*(7), 1549–1561. https://doi.org/10.5194/se-12-1549-2021

Dohmen, J., Schmeling, H., & Kruse, J. P. (2019). The effect of effective rock viscosity on 2-d magmatic porosity waves. *Solid Earth*, *10*(6), 2103–2113. https://doi.org/10.5194/se-10-2103-2019

Faul, U. H., & Jackson, I. (2007). Diffusion creep of dry, melt-free olivine. *Journal of Geophysical Research: Solid Earth*, *112*(B4). https://doi.org/10.1029/2006jb004586

Fowler, A. C., & Yang, X. (1999). Pressure solution and viscous compaction in sedimentary basins. *Journal of Geophysical Research*, *104*(B6), 12989–12997. https://doi.org/10.1029/1998jb900029

Glatzmaier, G. A. (1988). Numerical simulations of mantle convection - Time-dependent, 3-dimensional, compressible, spherical-shell. *Geophysical & Astrophysical Fluid Dynamics*, *43*(2), 223–264. https://doi.org/10.1080/03091928808213626

Hilbert, D., & Cohn-Vossen, S. (1952). *Geometry and the imagination*. Illus.-VII. 357.

Hirth, G., & Kohlstedt, D. L. (1995). Experimental constraints on the dynamics of the partially molten upper-mantle—Deformation in the diffusion creep regime. *Journal of Geophysical Research: Solid Earth*, *100*(B2), 1981–2001. https://doi.org/10.1029/94jb02128

Hirth, G., & Kohlstedt, D. L. (2003). Rheology of the upper mantle and mantle wedge: A view from the experimentalists. In J. M. Eiler (Ed.) *Inside the subduction factory* (pp. 83–105). American Geophysical Union. https://doi.org/10.1029/138gm06

Holtzman, B. K. (2016). Questions on the existence, persistence, and mechanical effects of a very small melt fraction in the asthenosphere. *Geochemistry, Geophysics, Geosystems*, *17*(2), 470–484. https://doi.org/10.1002/2015gc006102

Irvine, T. N. (1975). Crystallization sequences in musk-ox intrusion and other layered intrusions .2. Origin of chromitite layers and similar deposits of other magmatic ores. *Geochimica et Cosmochimica Acta*, *39*(6–7), 991–1020. https://doi.org/10.1016/0016-7037(75)90043-5

Irvine, T. N. (1980). Magmatic density currents and cumulus processes. *American Journal of Science*, *280*, 1–58.

Jackson, M. D., Blundy, J., & Sparks, R. S. J. (2018). Chemical differentiation, cold storage and remobilization of magma in the Earth's crust. *Nature*, *564*(7736), 405–409. https://doi.org/10.1038/s41586-018-0746-2

Jaeger, H. M., & Nagel, S. R. (1992). Physics of the granular state. *Science*, *255*(5051), 1523–1531. https://doi.org/10.1126/science.255.5051.1523

Jones, S. M., & Maclennan, J. (2005). Crustal flow beneath Iceland. *Journal of Geophysical Research: Solid Earth*, *110*(B9). https://doi.org/10.1029/2004jb003592

Jordan, J. S., Hesse, M. A., & Rudge, J. F. (2018). On mass transport in porosity waves. *Earth and Planetary Science Letters*, *485*, 65–78. https://doi.org/10.1016/j.epsl.2017.12.024

Keller, T., & Suckale, J. (2019). A continuum model of multi-phase reactive transport in igneous systems. *Geophysical Journal International*, *219*(1), 185–222. https://doi.org/10.1093/gji/ggz287

Kilburn, M. R., & Wood, B. J. (1997). Metal-silicate partitioning and the incompatibility of S and SI during core formation. *Earth and Planetary Science Letters*, *152*(1–4), 139–148. https://doi.org/10.1016/s0012-821x(97)00125-8

Krattli, G., & Schmidt, M. W. (2021). Experimental settling, floatation and compaction of plagioclase in basaltic melt and a revision of melt density. *Contributions to Mineralogy and Petrology*, *176*(4), 30. https://doi.org/10.1007/s00410-021-01785-6

Manoochehri, S., & Schmidt, M. W. (2014). Settling and compaction of chromite cumulates employing a centrifuging piston cylinder and application to layered mafic intrusions. *Contributions to Mineralogy and Petrology*, *168*(6), 1091. https://doi.org/10.1007/s00410-014-1091-6

Marquart, G., Schmeling, H., & Braun, A. (1999). Small-scale instabilities below the cooling oceanic lithosphere. *Geophysical Journal International*, *138*(3), 655–666. https://doi.org/10.1046/j.1365-246x.1999.00885.x

McKenzie, D. (1984). The generation and compaction of partially molten rock. *Journal of Petrology*, *2*(3), 713–765. https://doi.org/10.1093/petrology/25.3.713

McKenzie, D. (1985). The extraction of magma from the crust and mantle. *Earth and Planetary Science Letters*, *74*(1), 81–91. https://doi.org/10.1016/0012-821x(85)90168-2

McKenzie, D. (1987). The compaction of igneous and sedimentary rocks. *Journal of the Geological Society London*, *144*(2), 299–307. https://doi.org/10.1144/gsjgs.144.2.0299

McKenzie, D. (2011). Compaction and crystallization in magma chambers: Towards a model of the skaergaard intrusion. *Journal of Petrology*, *52*(5), 905–930. https://doi.org/10.1093/petrology/egr009

Mei, S., Bai, W., Hiraga, T., & Kohlstedt, D. L. (2002). Influence of melt on the creep behavior of olivine-basalt aggregates under hydrous conditions. *Earth and Planetary Science Letters*, *201*(3–4), 491–507. https://doi.org/10.1016/s0012-821x(02)00745-8

Mondal, S. K., & Mathez, E. A. (2007). Origin of the UG2 chromitite layer, bushveld complex. *Journal of Petrology*, *48*(3), 495–510. https://doi.org/10.1093/petrology/egl069

Morgan, J. P., & Smith, W. H. F. (1992). Flattening of the sea-floor depth age curve as a response to asthenospheric flow. *Nature*, *359*(6395), 524–527. https://doi.org/10.1038/359524a0

Nye, J. F. (1953). The flow law of ice from measurements in glacier tunnels, laboratory experiments and the Jungfraufirn borehole experiment. *Proceedings of the Royal Society of London*, *219A*, 477–489.

Raj, R. (1982). Creep in polycrystalline aggregates by matter transport through a liquid-phase. *Journal of Geophysical Research*, *87*(NB6), 4731–4739. https://doi.org/10.1029/JB087iB06p04731

Renner, J., Viskupic, K., Hirth, G., & Evans, B. (2003). Melt extraction from partially molten peridotites. *Geochemistry, Geophysics, Geosystems*, *4*(5). https://doi.org/10.1029/2002gc000369

Richardson, J. F., & Zaki, W. N. (1954). The sedimentation of a suspension of uniform spheres under conditions of viscous flow. *Chemical Engineering Science*, *3*(2), 65–73. https://doi.org/10.1016/0009-2509(54)85015-9

Richter, F. M., & McKenzie, D. (1984). Dynamical models for melt segregation from a deformable rock matrix. *The Journal of Geology*, *92*(6), 729–740. https://doi.org/10.1086/628908

Rubin, K. H., van der Zander, I., Smith, M. C., & Bergmanis, E. C. (2005). Minimum speed limit for ocean ridge magmatism from Pb-210-Ra-226-Th-230 disequilibria. *Nature*, *437*(7058), 534–538. https://doi.org/10.1038/nature03993

Rudge, J. F. (2018). The viscosities of partially molten materials undergoing diffusion creep. *Journal of Geophysical Research: Solid Earth*, *123*(12), 10534–10562. https://doi.org/10.1029/2018jb016530

Rudge, J. F. (2021). A micropolar continuum model of diffusion creep. *Philosophical Magazine*, *101*(17), 1913–1941. https://doi.org/10.1080/14786435.2021.1946191

Rutter, E. H. (1976). Kinetics of rock deformation by pressure solution. *Philosophical Transactions of the Royal Society A: Mathematical, Physical & Engineering Sciences*, *283*(1312), 203–219. https://doi.org/10.1098/rsta.1976.0079

Rybacki, E., & Dresen, G. (2004). Deformation mechanism maps for feldspar rocks. *Tectonophysics*, *382*(3–4), 173–187. https://doi.org/10.1016/j.tecto.2004.01.006

Schmeling, H., Kruse, J. P., & Richard, G. (2012). Effective shear and bulk viscosity of partially molten rock based on elastic moduli theory of a fluid filled poroelastic medium. *Geophysical Journal International*, *190*(3), 1571–1578. https://doi.org/10.1111/j.1365-246X.2012.05596.x

Schmidt, M. W., Forien, M., Solferino, G., & Bagdassarov, N. (2012). Settling and compaction of olivine in basaltic magmas: An experimental study on the time scales of cumulate formation. *Contributions to Mineralogy and Petrology*, *164*(6), 959–976. https://doi.org/10.1007/s00410-012-0782-0

Scott, D. R., & Stevenson, D. J. (1984). Magma solitons. *Geophysical Research Letters*, *11*(11), 1161–1164. https://doi.org/10.1029/gl011i011p01161

Scott, D. R., & Stevenson, D. J. (1986). Magma ascent by porous flow. *Journal of Geophysical Research: Solid Earth and Planets*, *91*(B9), 9283–9296. https://doi.org/10.1029/jb091ib09p09283

Selway, K., Smirnov, M. Y., Beka, T., O'Donnell, J. P., Minakov, A., Senger, K., et al. (2020). Magnetotelluric constraints on the temperature, composition, partial melt content, and viscosity of the upper mantle beneath Svalbard. *Geochemistry, Geophysics, Geosystems*, *21*(5). https://doi.org/10.1029/2020gc008985

Shimizu, I. (1995). Kinetics of pressure solution creep in quartz; theoretical considerations. *Tectonophysics*, *245*(3–4), 121–134. https://doi.org/10.1016/0040-1951(94)00230-7

Shirley, D. N. (1986). Compaction of igneous cumulates. *The Journal of Geology*, *94*(6), 795–809. https://doi.org/10.1086/629088

Skarbek, R. M., & Rempel, A. W. (2016). Dehydration-induced porosity waves and episodic tremor and slip. *Geochemistry, Geophysics, Geosystems*, *17*(2), 442–469. https://doi.org/10.1002/2015gc006155

Solano, J. M. S., Jackson, M. D., Sparks, R. S. J., & Blundy, J. (2014). Evolution of major and trace element composition during melt migration through crystalline mush: Implications for chemical differentiation in the crust. *American Journal of Science*, *314*(5), 895–939. https://doi.org/10.2475/05.2014.01

Solferino, G. (2008). *Melt extraction, permeability, and textural development during melting at high pressures: Experimentation to 1000 g in a centrifuging piston cylinder (maximum 1 gpa, 1400 C)*, ETH-Zurich. 164. https://doi.org/10.3929/ethz-a-005673192

Sparks, R. S. J., Annen, C., Blundy, J. D., Cashman, K. V., Rust, A. C., & Jackson, M. D. (2019). Formation and dynamics of magma reservoirs. *Philosophical Transactions of the Royal Society A: Mathematical, Physical & Engineering Sciences*, *377*(2139), 20180019. https://doi.org/10.1098/rsta.2018.0019

Sparks, R. S. J., Huppert, H. E., Kerr, R. C., McKenzie, D. P., & Tait, S. R. (1985). Postcumulus processes in layered intrusions. *Geological Magazine*, *122*(5), 555–568. https://doi.org/10.1017/s0016756800035470

Stocker, R. L., & Ashby, M. F. (1973). Rheology of upper mantle. *Reviews of Geophysics*, *11*(2), 391–426. https://doi.org/10.1029/RG011i002p00391

Suetnova, E., & Vasseur, G. (2000). 1-d modelling rock compaction in sedimentary basins using a visco-elastic rheology. *Earth and Planetary Science Letters*, *178*(3–4), 373–383. https://doi.org/10.1016/s0012-821x(00)00074-1

Sumita, I., Yoshida, S., Kumazawa, M., & Hamano, Y. (1996). A model for sedimentary compaction of a viscous medium and its application to inner-core growth. *Geophysical Journal International*, *124*(2), 502–524. https://doi.org/10.1111/j.1365-246x.1996.tb07034.x

Suzuki, A. M., Yasuda, A., & Ozawa, K. (2008). Cr and al diffusion in chromite spinel: Experimental determination and its implication for diffusion creep. *Physics and Chemistry of Minerals*, *35*(8), 433–445. https://doi.org/10.1007/s00269-008-0238-2

Swinkels, F. B., Wilkinson, D. S., Arzt, E., & Ashby, M. F. (1983). Mechanisms of hot-isostatic pressing. *Acta Metallurgica*, *31*(11), 1829–1840. https://doi.org/10.1016/0001-6160(83)90129-3

Takei, Y. (2017). Effects of partial melting on seismic velocity and attenuation: A new insight from experiments. In R. Jeanloz & K. H. Freeman (Eds.) *Annual review of Earth and planetary sciences* (Vol. 45, pp. 447–470). https://doi.org/10.1146/annurev-earth-063016-015820

Takei, Y., & Holtzman, B. K. (2009a). Viscous constitutive relations of solid-liquid composites in terms of grain boundary contiguity: 1. Grain boundary diffusion control model. *Journal of Geophysical Research: Solid Earth*, *114*(B6), B06205. https://doi.org/10.1029/2008jb005850

Takei, Y., & Holtzman, B. K. (2009b). Viscous constitutive relations of solid-liquid composites in terms of grain boundary contiguity: 2. Compositional model for small melt fractions. *Journal of Geophysical Research: Solid Earth*, *114*(B6), B06206. https://doi.org/10.1029/2008jb005851

Takei, Y., & Katz, R. F. (2013). Consequences of viscous anisotropy in a deforming, two-phase aggregate. Part 1. Governing equations and linearized analysis. *Journal of Fluid Mechanics*, *734*, 424–455. https://doi.org/10.1017/jfm.2013.482

Tegner, C., Thy, P., Holness, M. B., Jakobsen, J. K., & Lesher, C. E. (2009). Differentiation and compaction in the skaergaard intrusion. *Journal of Petrology*, *50*(5), 813–840. https://doi.org/10.1093/petrology/egp020

Tomkins, M. R., Baldock, T. E., & Nielsen, P. (2005). Hindered settling of sand grains. *Sedimentology*, *52*(6), 1425–1432. https://doi.org/10.1111/j.1365-3091.2005.00750.x

Tumarkina, E., Misra, S., Burlini, L., & Connolly, J. A. D. (2011). An experimental study of the role of shear deformation on partial melting of a synthetic metapelite. *Tectonophysics*, *503*(1–2), 92–99. https://doi.org/10.1016/j.tecto.2010.12.004

Vergnolle, M., Pollitz, F., & Calais, E. (2003). Constraints on the viscosity of the continental crust and mantle from GPS measurements and postseismic deformation models in western Mongolia. *Journal of Geophysical Research: Solid Earth*, *108*(B10). https://doi.org/10.1029/2002jb002374

Vigneresse, J. L., Barbey, P., & Cuney, M. (1996). Rheological transitions during partial melting and crystallization with application to felsic magma segregation and transfer. *Journal of Petrology*, *37*(6), 1579–1600. https://doi.org/10.1093/petrology/37.6.1579

Wilkinson, D. S., & Ashby, M. F. (1975). Pressure sintering by power law creep. *Acta Metallurgica*, *23*(11), 1277–1285. https://doi.org/10.1016/0001-6160(75)90136-4

Yamasaki, T., & Kobayashi, T. (2018). Imaging a low viscosity zone beneath the Kutcharo Caldera, eastern Hokkaido, Japan, using geodetic data. *Earth and Planetary Science Letters*, *504*, 1–12. https://doi.org/10.1016/j.epsl.2018.09.038